An ALMA CO(1-0) survey of the 2Jy sample: large and massive molecular discs in radio AGN host galaxies

C. Tadhunter,[1]* T. Oosterloo,[2,3] R. Morganti [ORCID],[2,3] C. Ramos Almeida [ORCID],[4,5] M. Villar Martín [ORCID],[6] B. Emonts [ORCID][7] and D. Dicken [ORCID][8]

[1]*Department of Physics and Astronomy, University of Sheffield, Sheffield S7 3RH, UK*
[2]*ASTRON, the Netherlands Institute for Radio Astronomy, Oude Hoogeveensedijk 4, NL-7991 PD Dwingeloo, the Netherlands*
[3]*Kapteyn Astronomical Institute, University of Groningen, Postbus 800, NL-9700 AV Groningen, the Netherlands*
[4]*Instituto de Astrofísica de Canarias, Calle Vía Láctea, s/n, E-38205 La Laguna, Tenerife, Spain*
[5]*Departamento de Astrofísica, Universidad de La Laguna, E-38205 La Laguna, Tenerife, Spain*
[6]*Centro de Astrobiología (CSIC-INTA), Carretera de Ajalvir, km 4, E-28850 Torrejón de Ardoz, Madrid, Spain*
[7]*National Radio Astronomy Observatory, 520 Edgemont Road, Charlottesville, VA 22903, USA*
[8]*UK Astronomy Technology Centre, Royal Observatory Edinburgh, Blackford Hill, Edinburgh EH9 3HJ, UK*

ABSTRACT

The jets of radio AGN provide one of the most important forms of active galactic nuclei (AGN) feedback, yet considerable uncertainties remain about how they are triggered. Since the molecular gas reservoirs of the host galaxies can supply key information about the dominant triggering mechanism(s), here we present Atacama Large Millimeter/sub-millimeter Array CO(1-0) observations of a complete sample of 29 powerful radio AGN ($P_{1.4\,\mathrm{GHz}} > 10^{25}\,\mathrm{W\,Hz^{-1}}$ and $0.05 < z < 0.3$) with an angular resolution of about 2–3 arcsec (corresponding to 2–8 kpc). We detect molecular gas with masses in the range $10^{8.9} < M_{\mathrm{H_2}} < 10^{10.2}\,\mathrm{M_\odot}$ in the early-type host galaxies of ten targets, while for the other 19 sources, we derive upper limits. The detection rate of objects with such large molecular masses – 34 ± 9 per cent – is higher than in the general population of non-active early-type galaxies (ETGs: <10 per cent). The kinematics of the molecular gas are dominated in most cases by rotating disc-like structures, with diameters up to 25 kpc. Compared with the results for samples of quiescent ETG in the literature, we find a larger fraction of more massive, more extended and less settled molecular gas structures. In most of the CO-detected sources, the results are consistent with triggering of the AGN as the gas settles following a merger or close encounter with a gas-rich companion. However, in a minority of objects at the centres of rich clusters of galaxies, the accretion of gas cooling from the hot X-ray haloes is a plausible alternative to galaxy interactions as a triggering mechanism.

Key words: galaxies: active – galaxies: interactions – galaxies: jets – radio lines: galaxies.

1 INTRODUCTION

The origin of the activity from a supermassive black hole (SMBH) and its impact on the host galaxy continue to be topics of extreme interest in extragalactic astronomy. This is due to the importance of understanding the phenomena involved and to the fact that growing SMBH, known as active galactic nuclei (AGN), are considered a key element in the evolution of galaxies of all types (e.g. Fabian 1999; Veilleux, Cecil & Bland-Hawthorn 2005; King & Pounds 2015; Harrison et al. 2018). Not only are they likely to be triggered as a consequence of gas infall as galaxies evolve, but there is growing evidence that they also directly influence the evolution of their host galaxies via the feedback effects of their jets and winds. Clearly, if we are to properly incorporate AGN into galaxy evolution models, it is crucial to understand the symbiosis between AGN and their host galaxies and, in particular, the presence and properties of the fuelling gas (e.g. García-Burillo et al. 2021; Ramos Almeida et al. 2022).

In this context, radio AGN ($P_{1.4\,\mathrm{GHz}} > 10^{24}\,\mathrm{W\,Hz^{-1}}$) are particularly important, because their relativistic jets are known to couple efficiently with the hot IGM/ICM on scales of 10 kpc–1 Mpc and directly affect its cooling (Best et al. 2006; McNamara & Nulsen 2012). This is arguably the most important form of AGN-induced feedback in the local universe in terms of overall impact on galaxy evolution; however, radio jets can also affect the interstellar medium (ISM) of their host galaxies on smaller, (sub-)kpc scales (see e.g. Holt, Tadhunter & Morganti 2008; Mukherjee et al. 2016; Morganti et al. 2021; Girdhar et al. 2022; Murthy et al. 2022; Audibert et al. 2023, and many others). Moreover, radio AGN are invariably associated with massive ($M_* \gtrsim 10^{11}\,\mathrm{M_\odot}$) early-type galaxies (ETG), making it easier to search for the signs of the triggering events such as tidal features, recent star formation activity, and accreted gas reservoirs.

Considerable recent progress has been made in understanding the triggering of radio AGN. In particular, deep optical imaging studies have demonstrated that a majority (65–95 per cent) of powerful

* E-mail: c.tadhunter@sheffield.ac.uk

2Jy and 3CR radio sources with strong, quasar-like emission lines – here labelled strong-line radio galaxies (SLRGs)[1] – show high surface brightness tidal features or double nuclei, consistent with the triggering of their AGN in galaxy interactions (Ramos Almeida et al. 2011; Pierce et al. 2022). In contrast, weak-line radio galaxies (WLRGs) show a lower incidence of tidal features, and may be fuelled instead by accretion of gas cooling from the hot halo (Ruffa et al. 2019a; Maccagni et al. 2021; Oosterloo, Morganti & Murthy 2024), or by the direct accretion of hot gas from the halo (Hardcastle, Evans & Croston 2007).

Further information about the triggering mechanisms is provided by deep *Herschel* far-IR observations of the 2Jy sample which allow the cool ISM contents (using dust masses as a proxy) and star formation rates (SFR) of the host galaxies to be quantified. Consistent with the trends seen in the optical morphology results, it is found that SLRG have both higher dust masses and SFR than WLRG (Bernhard et al. 2022), reinforcing the idea that the SLRG are triggered by cool gas accreted in galaxy interactions, but that the fuelling gas in many WLRG may have a different origin. However, for most of the 2Jy objects the *Herschel* detections only extend to 160 μm, and may miss the emission from the coolest dust ($T_{dust} < 20$ K), especially in the presence of synchrotron emission from the radio cores, which can extend to mm and far-IR wavelengths and be strong in some cases (Dicken et al. 2023). Moreover, the low spatial resolution *Herschel* observations (FWHM ~12 arcsec at 160 μm) give no information on the distribution and kinematics of the cool ISM, which are key for understanding the origins of the gas and the triggering of the activity. Therefore, for a full picture of the triggering of radio AGN, it is important to obtain CO observations of the molecular gas, which directly probe the masses, distributions and kinematics of the cool ISM.

Pre-ALMA CO surveys of samples of powerful radio AGN in the local universe detected substantial molecular gas reservoirs in some objects (Evans et al. 2005; Ocaña Flaquer et al. 2010; Smolčić & Riechers 2011), but lacked the spatial resolution necessary to map the distribution and kinematics of the gas, which are key for understanding its origins and interplay with the radio plasma. Therefore, the higher spatial resolution and sensitivity offered by mm interferometers like ALMA have the potential to lead to a major step forward in this field. Spatially resolved observations of molecular gas in powerful radio AGN are still limited to a small number of local objects in modest samples (e.g. Ruffa et al. 2019a; Audibert et al. 2022) or studies of single objects (e.g. some of the more recent additions are Morganti et al. 2015; Espada et al. 2017; Oosterloo et al. 2019, 2024; Rose et al. 2019; Maccagni et al. 2021; Morganti et al. 2021; Carilli et al. 2022), in some cases observed with high (sub-arcsec) angular resolution. In addition, particular attention has been given to tracing the molecular gas in and around radio AGN in (cool core) clusters (see e.g. Tremblay et al. 2016; Russell et al. 2019; Rose et al. 2020, and reference therein). In such systems, the mass and radial extent of the molecular gas can be particularly large and only in a minority of cases displays a clear and regular rotation (see e.g. Rose et al. 2019).

These observations have already shown the presence of massive molecular gas discs (see e.g. Rose et al. 2019; Ruffa et al. 2019a,

b, 2020; Audibert et al. 2022) in a significant fraction of nearby radio AGN, but also gas with disturbed kinematics suggestive of the infall of clouds in some cases (e.g. Tremblay et al. 2016; Maccagni et al. 2018, 2021), and signs of molecular outflows (e.g. Morganti et al. 2015, 2021; Oosterloo et al. 2017, 2019; Murthy et al. 2022) in others. However, CO studies of radio AGN have sometimes been done in a piecemeal way, with most concentrating on nearby ($z <$ 0.05) radio AGN which have relatively low radio powers ($P_{1.4GHz} < 10^{25.5}$ W Hz^{-1}). It is now important to extend such studies to larger samples that encompass more powerful radio sources, to identify whether differences in the occurrence and properties of the molecular gas are present, thereby allowing a systematic investigation of how the molecular gas contents relate to host galaxy and AGN properties.

To reach this goal, here we present ALMA Cycle 7 CO(1-0) observations of a complete sample of 29 nearby ($0.05 < z < 0.3$), powerful ($10^{25} < P_{1.4GHz} < 10^{27.5}$ W Hz^{-1}) 2Jy radio AGN that are a factor of ~3–100 deeper in rms sensitivity than previous CO(1-0) observations of samples of powerful radio AGN, and have an angular resolution (~2.1–2.9 arcsec) that is high enough to trace the gas distribution and kinematics. We target the CO(1-0) transition, because it is less affected by excitation conditions than the higher CO transitions, and is thus the most reliable tracer of the overall molecular gas mass. The sample and observations are described in Sections 2 and 3, respectively, and the main results in Section 4. This is followed by a comparison with the results from other samples of radio AGN, quasars, and ETG in Section 5, and a discussion that puts the results in the context of the triggering of radio AGN in Section 6. Finally, the conclusions are presented in Section 7. All distances, spatial scales, and luminosities were calculated assuming a flat universe with $\Omega_M = 0.286$, $\Omega_{vac} = 0.714$, and $H_\circ = 69.6$ km s^{-1} Mpc^{-1}.

2 THE SAMPLE AND ITS MULTIWAVELENGTH PROPERTIES

The sample used in this work is a complete sub-set of the full 2Jy sample of 46 southern radio galaxies with intermediate redshifts $0.05 < z < 0.7$, high 2.7-GHz radio fluxes $S_{2.7 GHz} > 2$Jy, southerly declinations $\delta < +10°$, and steep radio spectral indices $\alpha > 0.5$ (for $F_\nu \propto \nu^{-\alpha}$), as presented in Tadhunter et al. (1998) and Dicken et al. (2009). The radio source, AGN and host galaxy properties of this sample are well characterized by a rich set of multiwavelength data: All objects have deep ESO2.2m, ESO3.6m, New Technology Telescope or Very Large Telescope optical spectra (Tadhunter et al. 1993; Holt et al. 2007), Gemini r'-band images (Ramos Almeida et al. 2011, 2013), *Spitzer*/MIPS and *Herschel*/PACS mid- to far-IR photometry (Dicken et al. 2008, 2009, 2023; Tadhunter et al. 2014), and high- and low-frequency VLA/ATCA radio maps (Morganti, Killeen & Tadhunter 1993; Dicken et al. 2008); 98 per cent have deep *Chandra* or *XMM* X-ray data (Mingo et al. 2014); 90 per cent have deep *Spitzer*/IRS mid-IR spectra (Dicken et al. 2012).

For this project to observe CO(1-0), we have selected a complete sub-set of all 29 2Jy sources with redshifts in the range $0.05 < z < 0.3$. For one target, Hydra A (PKS0915–11), sufficiently deep CO(1-0) ALMA observations already existed and have been presented in (Rose et al. 2019, ref.: ADS/JAO.ALMA#2016.1.01214.S, ADS/JAO.ALMA#2017.1.00629.S). We observed the remaining 28 objects in our Cycle 7 ALMA project (ref: ADS/JAO.ALMA#2019.1.01022.S). Basic information about the targets and their ALMA observations is given in Table 1.

The upper redshift limit is chosen to ensure that the objects are at sufficiently low redshift to be confident of detecting CO(1-0)

---

[1] Formally SLRG are defined to have high [O III]λ5007 equivalent widths (EW$_{[O III]}$ > 10 Å), in contrast to WLRG, which have low [O III]λ5007 equivalent widths (EW$_{[O III]}$ < 10 Å) (Tadhunter et al. 1998). The SLRG and WLRG classes are similar to, but not exactly the same as, high-excitation radio galaxies (HERGs) and low-excitation radio galaxies (LERGs), respectively (see Tadhunter 2016).

Table 1. Basic target information, redshifts and observation details.

	Alternative name	Optical class	Radio class	Enviroment	$L_{\text{[O III]}}$ log (W)	z	T_{obs} (s)	rms$_{\text{cont}}$ (mJy b^{-1})	rms$_{\text{CO}}$ (mJy b^{-1})	Beam (arcsec)
PKS0034–01	3C 15	WLRG	FRI/FRII	G/I	33.5	0.073	1663	0.10	0.25	2.26×1.82
PKS0035–02	3C 17	SLRG	FRII	G/I	35.1	0.22	695	0.49	0.46	2.60×2.04
PKS0038+09	3C 18	SLRG	FRII	G/I	35.2	0.188	1482	0.11	0.28	2.23×1.75
PKS0043–42		WLRG	FRII	G/I	33.7	0.116	1512	0.03	0.33	2.42×1.80
PKS0213–13		SLRG	FRII	G/I	35.1	0.147	1421	0.04	0.32	2.40×1.96
PKS0349–27		SLRG	FRII	G/I	33.7	0.066	847	0.03	0.44	2.51×1.70
PKS0404+03	3C 105	SLRG	FRII	G/I	34.5	0.089	847	0.02	0.41	2.27×1.97
PKS0442–28		SLRG	FRII	G/I	34.8	0.147	1391	0.05	0.28	2.31×1.98
PKS0620–52		WLRG	FRI	C	<32.4	0.051	1935	0.16	0.33	2.18×1.96
PKS0625–35		WLRG	FRI	C	33.5	0.055	1724	0.15	0.24	2.17×1.89
PKS0625–53		WLRG	FRI	C	<33.1	0.054	1905	0.05	0.33	2.12×2.00
PKS0806–10		SLRG	FRII	G/I	35.8	0.10899^a	393	0.03	0.59	2.93×2.38
PKS0945+07	3C 227	SLRG	FRII	G/I	34.9	0.086	1663	0.02	0.31	2.22×1.87
PKS1151–34		SLRG	CSS	G/I	35.5	0.2579^b	696	0.35	0.44	2.84×1.82
PKS1559+02	3C 327	SLRG	CSS	G/I	35.3	0.104	393	0.05	0.60	2.44×2.03
PKS1648+05	3C 348	WLRG	FRI/FRII	C	33.7	0.1547^c	756	0.08	0.39	2.78×1.73
PKS1733–56		SLRG	FRII	G/I	34.8	0.098	424	0.17	0.56	2.22×1.88
PKS1814–63		SLRG	CSS	G/I	33.6	0.06374^b	514	0.07	0.64	2.27×1.93
PKS1839–48		WLRG	FRI	C	<32.4	0.112	1572	0.14	0.32	2.35×1.65
PKS1932–46		SLRG	FRII	G/I	35.4	0.2307^d	726	0.06	0.39	2.35×1.87
PKS1934–63		SLRG	GPS	G/I	35.1	0.1826^b	1572	0.10	0.28	2.20×1.97
PKS1949+02	3C 403	SLRG	FRII	G/I	34.9	0.0584^e	454	0.05	0.64	2.37×1.77
PKS1954–55		WLRG	FRI	C	<32.0	0.06	1875	0.10	0.31	2.17×2.04
PKS2135–14		SLRG	FRII	G/I	36.1	0.2	1361	0.07	0.33	2.84×1.60
PKS2211–17	3C 444	WLRG	FRII	C	33.4	0.153	726	0.03	0.43	2.82×1.56
PKS2221–02	3C 445	SLRG	FRII	G/I	35.2	0.057	1753	0.02	0.34	2.45×1.73
PKS2314+03	3C 459	SLRG	FRII	G/I	35.2	0.2199^b	363	0.05	0.58	2.33×1.92
PKS2356–61		SLRG	FRII	G/I	35.0	0.096	877	0.06	0.40	2.09×1.88
PKS0915–11	3C 218	WLRG	FRI	C	33.5	0.054	2700	–	0.21	Rose et al.

Notes. The redshifts of most of the observed galaxies are taken from Dicken et al. (2008), but those marked with *a*, *b*, *c*, *d*, and *e* are taken from the 6dF redshift survey, Santoro et al. (2020), Hamer et al. (2016), Inskip et al. (2007), and Koss et al. (2022), respectively. The third and fourth columns give the optical and radio classifications of the sources: WLRG (weak-line radio galaxy: EW[O III] < 10 Å); SLRG (strong-line radio galaxy: EW[O III] > 10 Å); FRI (Fanaroff–Riley class I); FRII (Fanaroff–Riley class II); FRI/FRII (hybrid radio morphology between FRI and FRII); CSS (compact steep spectrum radio source); and GPS (gigahertz-peaked radio source). The fifth column gives an indication of the large-scale environments of the sources: objects with extended ICM X-ray luminosities $L_{2–10\,\text{keV}} > 5 \times 10^{43}$ erg s^{-1} (as measured by Ineson et al. 2015) and/or an angular clustering amplitude $B_{\text{gq}} > 600$ (as measured by Ramos Almeida et al. 2013) are taken to be in relatively rich, cluster-like environments (indicated by 'C'); whereas objects not fulfilling these requirements are assumed to be in lower density group, or isolated, environments (indicated by 'G/I'). Note that the [O III] emission-line luminosities (sixth column) are taken from Dicken et al. (2023), and the CO rms values (tenth column) were calculated for a channel width of 30 km s^{-1}. The final column gives the major and minor axes of the restoring beam

in reasonable integration times in ALMA Band 3, while the lower redshift limit ensures that the objects host genuinely powerful radio sources. On the basis of their optical [O III] emission-line and 24-μm mid-IR continuum luminosities, the sample covers 2 orders of magnitude in bolometric luminosity for a given radio power, with 19 of the targets classified as SLRG and 10 objects classified as WLRG based on their optical spectra. In terms of radio classifications, 21 per cent are FRI, while the remaining 79 per cent are FRII, FRI/FRII, CSS (compact steep spectrum radio source) or GPS (gigahertz-peaked radio source) objects, see O'Dea & Saikia (2021) for a review of peaked-spectrum sources.

The angular resolution obtained by the observations presented here corresponds to ∼2 kpc for the lowest redshift objects in our sample, and increases to ∼8 kpc for the highest redshift in the sample. This resolution is sufficient to separate the CO emission of the radio AGN host galaxies from that of the companion galaxies that are present in many cases, thus providing a major advantage compared with previous single-dish CO observations. For one object, PKS2314+03 (3C 459), we also make use of higher spatial resolution (0.238 arcsec)

data available in the archive.[2] The latter data are used only for the modelling of the kinematics of the gas (see Section 4.3), whereas all other molecular gas properties for this source (e.g. molecular gas mass and extent) were derived from the lower resolution data.

3 OBSERVATIONS

The observations of CO(1-0) and the 3-mm continuum were obtained in Cycle 7 using ALMA with 46 antennas in its most compact configurations (C43-1 and C43-2), with a shortest baseline of 15 m and a maximum baseline of about 500 m. The observations were done during the period 2019 August 30 to 2019 November 14. The angular resolution of the observations (∼2.1–2.9 arcsec) was chosen to allow the observations to be sensitive to the detection of extended and low surface brightness molecular gas in a relative short-integration time. The on-source exposure times were set based on pre-

[2]ADS/JAO.ALMA#2018.1.00739.S, PI Balmaverde

existing information on the cool ISM contents in the targets provided by *Herschel*-derived dust mass estimates (Tadhunter et al. 2014; Bernhard et al. 2022), and assuming a factor of 100 conversion factor from dust mass to molecular gas mass.[3] The CO(1-0) observations of Hydra A, taken from the ALMA archive, were obtained with a comparable resolution (1.8 arcsec) and reach a noise level of 0.7 mJy beam^{-1} for a 2.7 km s^{-1} (Rose et al. 2019) velocity channel, equivalent to 0.22 mJy beam^{-1} for a 30 km s^{-1} velocity channel – slightly more sensitive than typically obtained for the rest of the sample.

The field of view (FoV) of ∼60 arcsec and relatively low spatial resolution allow the observations to be sensitive to extended emission (both line and continuum; most of the objects are extended radio galaxies). However, in some cases, the FoV was not large enough to trace the entire continuum emission. This does not affect the interpretation of the CO(1-0) results. The observations were done in Band 3, making use of the correlator in Frequency Division Mode using four spectral windows. The central frequency of the line spectral window was set to the redshifted frequency of the CO(1-0) observations (rest frequency 115.3 GHz), with a total bandwidth of 1.875 GHz. With the 3840 channels used we had a native velocity resolution of 1.4 km s^{-1}, but in the subsequent data-reduction channels were combined to make image cubes with 15 km s^{-1} velocity channels, and a velocity resolution better matching the observed line widths (see below). The remaining spectral windows, each 2-GHz wide covered by 128 channels, were centred on frequencies surrounding the line spectral window and were used for continuum imaging. The calibration was done in CASA (v5.1.1; CASA team et al. 2022), which includes the ALMA pipeline (v. r40896; Hunter et al. 2023), using the reduction scripts provided by the ALMA observatory.

The products (continuum and line cube) provided by the ALMA pipeline were found to be of sufficient quality to perform the analysis. In Table 1, we summarize, for each target, the observing times, restoring beams and rms noises of the final continuum images and line data cubes.

The cubes provided by the ALMA pipeline were made with a robust weighting of 0.5, resulting in an average size of the restoring beam of about 2 arcsec, and a rms noise ranging from 0.24 to 0.64 mJy beam^{-1} for a channel width of 30 km s^{-1}. The numbers are summarized in Table 1. The velocity resolution of ∼30 km s^{-1} (with the exact value depending on the redshift of the source) is the result of binning 10 channels and then Hanning smoothing the original cubes. For the modelling of the kinematics of the gas for the stronger detections, we have produced cubes with a lower velocity resolution (60 km s^{-1}) in order to increase the signal to noise

The cubes were visually inspected for the detection of CO(1-0). However, to make the analysis systematic, they were also run through the Source Finding Application (SoFiA),[4] see Serra et al. (2015) for details. This software performs spatial and velocity smoothing in order to optimize the search for detections. The set of smoothing kernels used comprises all combinations of smoothing with 0, 3, and 7 pixels spatially and in velocity, and we built the detection mask by using those voxels above the 3.5σ level in any of the smoothed cubes. All mask regions smaller than three pixels in any direction were discarded as being noise peaks. Following this, all masks were

dilated with two spatial pixels and 1 velocity channel in order to include faint emission at the edges of the masks. The moment images shown in Fig. A1 are those obtained by SoFiA after visually checking that the procedure gave reliable results.

The continuum images were produced by the ALMA pipeline by combining the three continuum spectral windows, The images were also produced using a robust weigthing of 0.5, resulting in a restoring beam of ∼2 arcsec and with rms noise ranging from ∼0.03 to ∼0.5 mJy beam^{-1} (see Table 1). The objects with high noise often have emission extending over the entire FoV (and in many cases beyond).

4 RESULTS

Of the 28 targets of the new ALMA observations, we have eight detections of CO(1-0) emission (and, in one case, also absorption) at the location of the host galaxy. The targets for which we have detected CO(1-0) are PKS0806–10, PKS1648+05, PKS1733–56, PKS1814–63 (where both emission and absorption are detected), PKS1942–46, PKS1949+02, PKS2211–17, and PKS2314+03. The case of PKS1934–63 is more uncertain (see below). For the CO-detected sources, the total (velocity-integrated) H$_2$ column densities derived from the CO maps are shown superimposed on the Gemini GMOS r'-band images of Ramos Almeida et al. (2011) in Fig. 1, and the velocity field and position–velocity (PV) images are presented in Fig. A1 in the Appendix.

The mm-continuum images of all targets (excluding the known CSS/GPS sources which are unresolved at the angular resolution of our observations) are shown in Fig. A2, while the fluxes of the unresolved cores measured from these images are presented in Dicken et al. (2023). A large fraction of the objects show extended continuum structures, consistent with those found at GHz frequencies (e.g. Morganti et al. 1993, 1999; Dicken et al. 2008). In some cases, the emission clearly extends beyond the FoV of ALMA, confirming the large structures already seen at lower frequencies.

We also detect CO(1-0) in one system (PKS1934–63, see Fig. 1) in which an on-going interaction is taking place between the host galaxy of the radio AGN and a close companion (separated by only about 3 arcsec (9 kpc) – see Roche et al. 2016; Santoro et al. 2018). At the resolution of our observations, it is difficult to disentangle how much of the CO is actually on the target, and most of the CO is located between the two objects; however, a tail reaching PKS1934–63 (including its central regions) appears to be present. Indeed, the end of the tail closest to the centre of PKS1934–63 has a CO velocity within ∼50 km s^{-1} of the systemic velocity of the radio galaxy host from Santoro et al. (2018) (see Fig. A1).

Based on these detections, and adding the literature results for Hydra A, which is part of the sample, we derive a detection rate for the confirmed cases of 10/29 = 34±9 per cent.[5] It is important to note that this detection rate is for objects with relatively high molecular masses, i.e. above $10^{8.9}$ M$_\odot$, as covered by the present observations – see discussion in Section 4.1 – and this should be considered when making the comparison with other samples of radio AGN and ETG, see below and Section 5.

As mentioned above, we detect a deep absorption against the continuum of PKS1814–63. This is a CSS source with two lobe-like structures separated by about 400 pc (Tzioumis et al. 2002; Morganti et al. 2011) and unresolved in our ALMA observations. A discussion

---

[3]This is consistent with the total gas-to-dust ratios of nearby galaxies of solar metallicity (e.g. Rémy-Ruyer et al. 2014; De Vis et al. 2019; Casasola et al. 2020) and a molecular-to-neutral hydrogen mass ratio of $M_{H_2}/M_{H_I} \sim 1$.
[4]https://github.com/SoFiA-Admin/SoFiA

[5]We have used binomial statistics to calculate the uncertainties on the proportions throughout this paper.
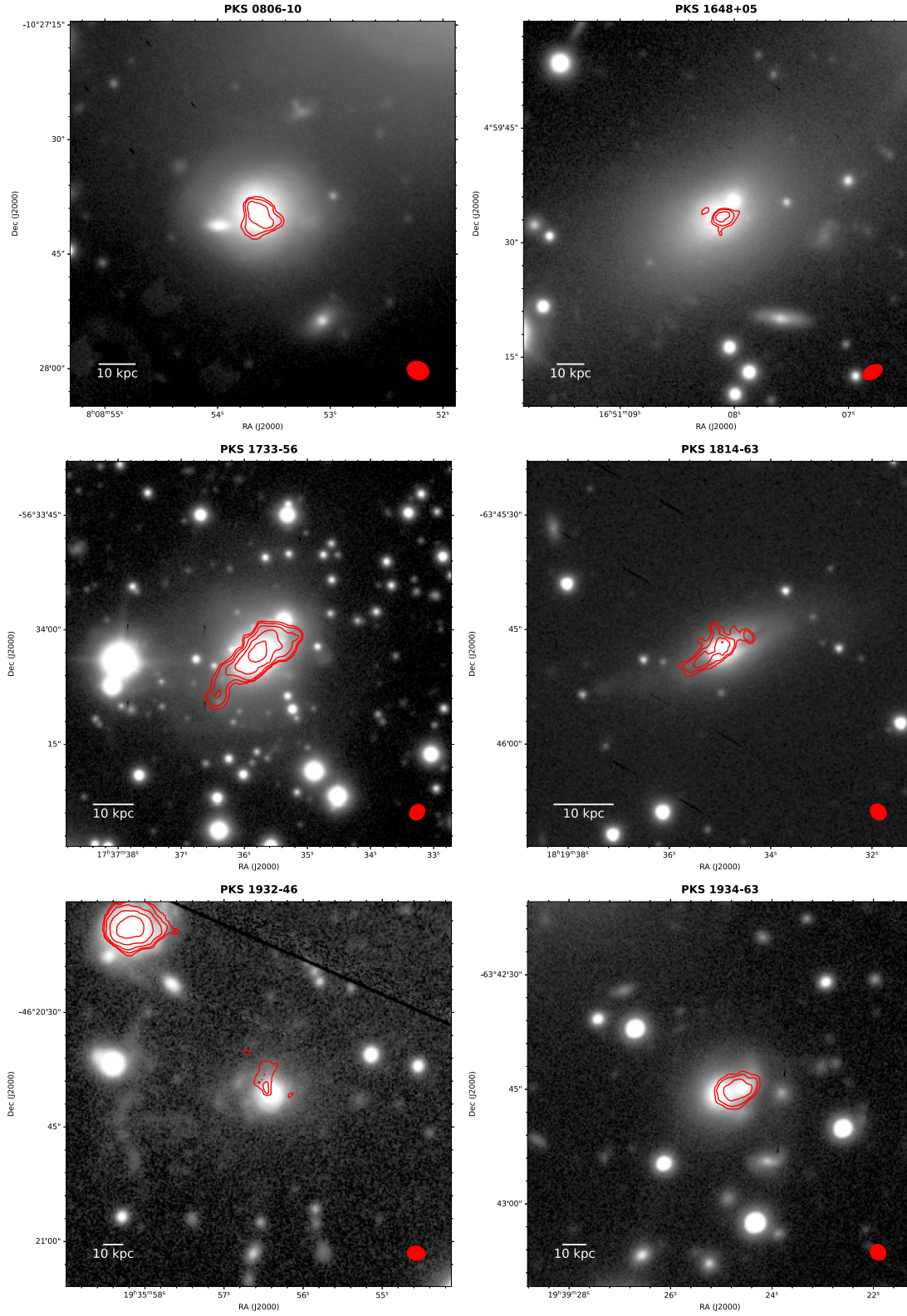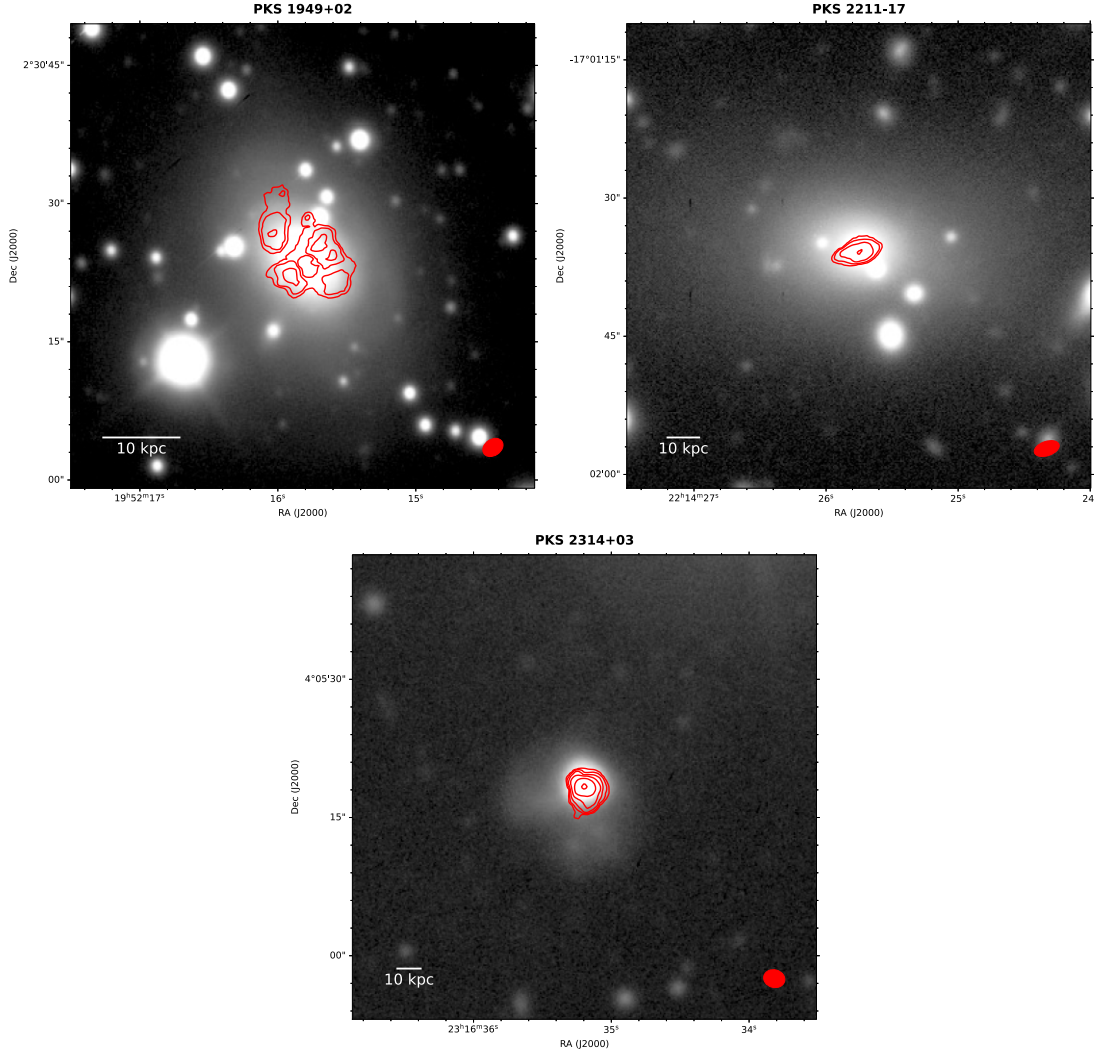
Figure 1. Total H_2 column density contours superimposed on Gemini GMOS r′ images from Ramos Almeida et al. (2011) for the CO-detected sources. H_2 contour levels are 1.5, 3, 6,...×10^{21} cm^{-2}. The red ellipses indicate the ALMA beam.

Figure 1. *– continued*

of the properties of the absorption and what we can learn from it is presented in Section 4.2.

Finally, in 10 fields, we detect CO(1-0) from associated companion galaxies ($|\Delta V| < 2500$ km s^{-1}). Particularly interesting is the case of PKS0620–52, where a companion galaxy is detected in CO(1-0) – with velocity blueshifted by about 1200 km s^{-1} compared to the systemic velocity of the target – at the location where the jet bends, $\sim$10 kpc ($\sim$10 arcsec) from the nucleus of the target (see Fig. A3). Determining whether an ongoing jet–cloud interaction is present, or the alignment with the bending of the jet is only a projection effect, will require deeper and higher resolution observations. The CO profile does not show extreme velocities, which might otherwise suggest the presence of an interaction. However, the limited S/N of the detection does not allow to completely rule out the presence of kinematically disturbed gas.

In 11 fields, we do not clearly detect any CO(1-0) emission either in the targets or in companion galaxies, although in one of these fields (PKS2221–02), there are two tentative detections of companions.

4.1 Masses of the molecular gas

The masses of the molecular gas were calculated using the standard formulae:

$$M_{\rm mol} = \alpha_{\rm CO} L'_{\rm CO} \qquad (1)$$

and

$$L'_{\rm CO} = 2453 \, S_{\rm CO} \, \Delta V \, D_{\rm L}^2/(1+z) \qquad (2)$$

with $S_{\rm CO}$ in Jy, $D_{\rm L}$ in Mpc, and ΔV in km s^{-1} in the emitters frame (i.e. de-redshifted velocities). The values of the H$_2$ masses presented in Table 2 have been obtained using $\alpha_{\rm CO} = 4.3$ M$_\odot$(K km s^{-1} pc^2)$^{-1}$ (corresponding to X$_{\rm CO} = 2 \times 10^{20}$ cm^{-2}(K km s^{-1})$^{-1}$). The choice of this value, which is typically assumed in the case of quiescent gas (Bolatto, Wolfire & Leroy 2013), has been motivated by the fact that, at least to first order, the structures observed in our sample appear to be mostly large discs with relatively regular kinematics (see Section 4.3); the same or a similar value for $\alpha_{\rm CO}$ has been assumed in many other CO studies of radio AGN (e.g. Ocaña Flaquer et al. 2010; Ruffa et al. 2019a) and quasars (Jarvis et al. 2020; Shangguan

Table 2. Molecular gas and cool dust mass estimates. Where CO(1-0) emission is detected, the uncertainties on the molecular gas masses include contributions from noise (estimated as $\delta(S_{CO}\Delta V)_{noise} = \sigma_{chan}\Delta V_{chan}\sqrt{\Delta V_{FWHM}/\Delta V chan}$, with $\Delta V_{FWHM}/\Delta V chan = 10$) and an assumed 5 per cent systematic flux calibration uncertainty (van Kempen et al. 2014), with these uncertainties added in quadrature.

	F (CO) (Jy km s^{-1})	M_{H_2} ($M_\odot/10^9$)	Limits $H_2{}^a$ $M_\odot$	Diameter kpc (arcmin)	Dust mass^b log($M_\odot$)	Gas/dust	Detections in field
PKS0034–01	–	–	1.3E + 08	–	<5.9	(160)	One companion
PKS0035–02	–	–	2.3E + 09	–	<7.3	(130)	No detection
PKS0038 + 09	–	–	1.0E + 09	–	<7.0	(100)	One companion
PKS0043-42	–	–	4.4E + 08	–	6.5	<140	No detection
PKS0213–13	–	–	6.9E + 08	–	6.5	<220	No detection
PKS0349–27	–	–	1.8E + 08	–	6.8	<32	No detection
PKS0404 + 03	–	–	3.2E + 08	–	6.5	<100	No detection
PKS0442–28	–	–	6.2E + 08	–	<6.5	(190)	One companion
PKS0620–52	–	–	8.2E + 07	–	<5.6	(210)	CO in companion along jet
PKS0625–35	–	–	7.0E + 07	–	<6.3	(34)	One companion
PKS0625–53	–	–	9.2E + 07	–	<5.4	(370)	One companion (+ two tentative)
PKS0806–10	0.55±0.06	1.35±0.15	–	10.5(5.2)	7.5	45	Detection
PKS0945+07	–	–	2.2E + 08	–	6.8	<40	No detection
PKS1151–34	–	–	3.0E + 09	–	7.6	<76	No detection
PKS1559+02	–	–	6.4E + 08	–	7.4	<24	One companion
PKS1648+05	0.25±0.04	1.25±0.19	–	11.2(4.5)	7.3	63	Detection
PKS1733–56	4.91±0.25	9.72±0.49	–	25.2(13.8)	7.9	130	Detection
PKS1814–63	1.02±0.09	0.84±0.08	–	13.3(10.8)	7.2	64	Detection with absorption
PKS1839–48	–	–	3.8E + 08	–	<6.2	(240)	One companion
PKS1932–46	0.20±0.04	2.33±0.44	–	16.4(4.4)	<7.2	>150	Detection, one companion
PKS1934–63	0.82±0.05	5.83±0.35	–	20.6(6.6)	7.6	150	CO in tail with companion
PKS1949+02	2.02±0.12	1.42±0.08	–	13.5(11.8)	7.3	73	Detection
PKS1954–55	–	–	1.1E + 08	–	<5.5	(340)	No detection
PKS2135-14	–	–	1.3E + 09	–	7.3	<69	No detection
PKS2211–17	0.51±0.06	2.53±0.25	–	14.2(5.3)	7.7	56	Detection
PKS2221–02	–	–	1.1E + 08	–	6.5	<35	Two tentative companions
PKS2314+03	1.73±0.10	18.1±1.1	–	11.7(3.2)^c	8.5	67	Detection
PKS2356–61	–	–	3.6E + 08	–	6.5	<110	No detection
PKS0915–11	1.81±0.09	1.06±0.05	–	4.5	6.9	140	From Rose et al. (2019)

^{a}Mass upper limits (5σ, one beam, $\Delta V_{FWHM} = 300$ km s^{-1}), see the text for details. ^{b}Dust masses from Bernhard et al. (2022). ^{c}The disc observed in the high spatial resolution cube is smaller, with a diameter of about 1 arcsec, i.e. 3.6 kpc. *Notes.* Note that uncertainties in the assumed value of α_{CO} have not been taken into account. For the gas/dust mass ratios in column 7, where both the dust mass and the gas mass are upper limits, the number is shown in brackets.

et al. 2020; Ramos Almeida et al. 2022). When making comparisons with other samples, all H_2 masses for objects from the other samples have been converted to this value.

The upper limits were derived using the relation:

$$S_{CO}\Delta V < 5\sigma_{chan}\Delta V_{chan}\sqrt{\frac{\Delta V_{FWHM}N_{beam}}{\Delta V_{chan}}}, \qquad (3)$$

where we assumed 5σ upper limits, a width of the expected profile of $\Delta V_{FWHM} = 300$ km s^{-1} for a channel width of $\Delta V_{chan} = 30$ kms^{-1}, and N_{beam} is the number of beams, initially assumed to have a value of 1. The 5σ could be considered quite conservative compared to other studies (e.g. both Smolčić & Riechers 2011 and Ruffa et al. 2019a use 3σ upper limits).

Fig. 2 shows how the molecular masses of the detections and upper limits are distributed as function of redshift. This plot demonstrates that the detections are not limited to the targets at low redshift. The figure also includes targets from Ruffa et al. (2019a) which fill the low redshift range. The comparison with this and other samples will be discussed in detail in Section 5.

Considering the lower end of the redshift range ($z < 0.12$), it is clear that the upper limits estimated by assuming the emission is spatially confined to one beam fall significantly below the detections of objects at similar redshifts. One possible explanation for this is that the assumption of one beam may be too optimistic. To
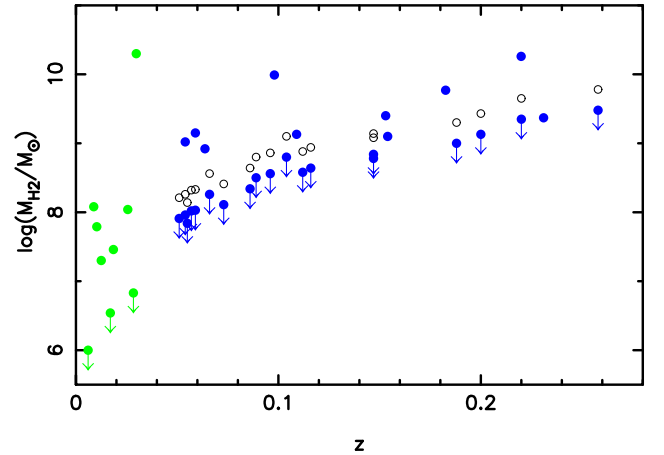

Figure 2. Distribution of the H_2 masses and limits as function of the redshift. The filled blue symbols represent the 2Jy detections, filled blue symbols with downward arrows represent 2Jy upper limits calculated assuming the CO emission covers one beam, and open grey symbols represent 2Jy upper limits calculated assuming four beams. Note that PKS1934–63 has been marked as detected in this and following plots, see Section 4 for details. The plot also includes the objects from Ruffa et al. (2019a) (filled green symbols) – a comparison between the two samples is presented in Section 5.

illustrate the effect of a more extended CO distribution, we also show as open black circles upper limits calculated by assuming that the molecular gas covers four beams – more consistent with the typical size of the observed CO(1-0) structures in the detected sources. With this even more conservative assumption, the upper limits fall closer to the detections, especially at the higher redshifts; however, there remains a gap between the upper limits and detections at the low redshift end. This may suggest a bimodal shape for the molecular gas mass distribution of radio AGN at low redshifts, but deeper observations of a larger sample would be required to confirm this. In the following, we assume that the emission is extended over one beam when calculating the upper limits for molecular gas masses.

Fig. 3 presents the distribution of the masses of the molecular gas (or limits) as function of [O III] luminosity (a proxy for the AGN bolometric luminosity: Heckman et al. 2004) and radio luminosity. There is no obvious trend with either [O III] or radio luminosity, and clearly radio AGN of given luminosity encompass a wide range of molecular gas mass ($\sim$1–2 orders of magnitude), echoing previous results based on *Herschel*-derived dust masses (Bernhard et al. 2022). This suggests that the mass of the molecular gas reservoir is not the sole determinant of the level of AGN and jet activity; other factors (e.g. the distribution of gas, and degree to which it is dynamically settled) must also be important.

For comparison, Fig. 3 top also includes the targets studied by Ruffa et al. (2019a), some well-known individual radio AGN, and results for samples of nearby radio-quiet type 1 and type 2 quasars (Shangguan et al. 2020; Ramos Almeida et al. 2022; Molyneux et al. 2024). At high [O III] luminosities, the radio AGN overlap with radio-quiet quasars: Clearly the hosts of some radio AGN are as gas-rich as radio-quiet quasars of similar [O III], perhaps reflecting a common origin for the gas in galaxy mergers (Husemann et al. 2017; Ramos Almeida et al. 2022; Pierce et al. 2023). However, it is also notable that the the 2Jy radio AGN sample shows a much a higher proportion of non-detections than the radio-quiet quasar samples, despite that fact that the rms sensitivity was similar to, or better than, than that of those samples (see Section 5).

4.2 Molecular gas detected in absorption

We detect deep and narrow CO(1-0) in absorption at the location of the peak of the continuum emission in PKS1814–63. Fig. 4 shows the absorption profile from the cube at full velocity resolution. Based on a double-Gaussian fit to the profile, the full width at half-maximum of the deep absorption is FWHM = 6.1 ± 0.1 km s^{-1}, and it is centred on the systemic velocity. The fitted depth of the absorption is 140 mJy against the continuum peak flux of 340 mJy. This corresponds to a peak optical depth of $\tau_{\text{peak}} = 0.53$. Interestingly, the profile also shows a broad component, with FWHM = 57.3 ± 5.3 km s^{-1} offset compared to the systemic velocity by $+18.0 \pm 3.7$ km s^{-1}. The peak depth of this feature is 8 mJy, corresponding to an optical depth of $\tau_{\text{peak}} = 0.024$.

The column density of the absorption was estimated following the standard formulae in Bolatto et al. (2013) and the approach described in Maccagni et al. (2018) and Morganti et al. (2021). The values were derived by assuming two extreme values for the excitation temperature (T_{ex}) of the gas. On the low side, the typical temperature of the CO gas in conditions of thermal equilibrium in the Milky Way is $\sim$16 K (e.g. Heyer et al. 2009). However, this temperature may be higher if the gas is affected by the AGN, as expected for gas located in the circumnuclear region. Temperatures up to $T_{\text{ex}}\sim$60 K have been reported in some cases (see Dasyra et al. 2014; Oosterloo et al. 2017).
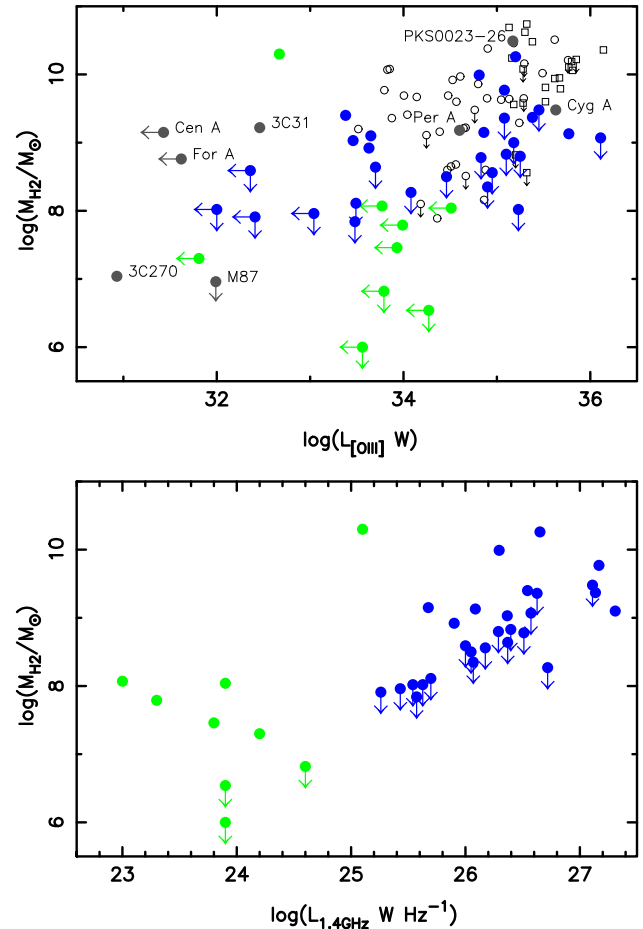

Figure 3. Top panel: molecular gas mass versus [O III]λ5007 luminosity for the 2Jy sample. In addition to the 2Jy (solid blue circles) and Ruffa et al. (2019a) (solid green circles) objects, for comparison we also show results for nearby type 2 quasars from Ramos Almeida et al. (2022) and Molyneux et al. (2024) (open black squares), type 1 quasars from Shangguan et al. (2020) (open black circles), and some well-known radio AGN from the literature (labelled, filled dark-grey cicles). The references for the individually labelled radio AGN are as follows: Cygnus A (Carilli et al. 2022), Fornax A (Maccagni et al. 2021), Centaurus A (Parkin et al. 2012), 3C270 (Boizelle et al. 2021), Perseus A (Bridges & Irwin 1998), 3C31 (North et al. 2019), M87 (Salome & Combes 2008), and PKS0023-26 (Morganti et al. 2021). Bottom panel: molecular gas mass versus radio luminosity for the 2Jy and Ruffa et al. (2019a) samples (same symbols as in the top plot). For the 2Jy sample, the [O III]λ5007 luminosities have been taken from Dicken et al. (2009), and the 1.4-GHz radio luminosities have been converted from the 5.0-GHz radio luminosities presented in that paper assuming a spectral index of $\alpha = 0.7$ (for $F_\nu \propto \nu^{-\alpha}$).

For example, a value of $T_{\text{ex}}\sim$42 K has been estimated by Rose et al. (2019) for Hydra A, a radio galaxy that belongs to the 2Jy sample. The H$_2$ column density derived for the deep absorption ranges from 2×10^{20} to 2×10^{21} cm^{-2} for excitation temperatures between 16 and 60 K, and a conversion factor CO-to-H$_2$ = 10^{-4}.[6] Similarly, we derive column densities in the range 9×10^{19} to 7×10^{20} cm^{-2} for the broad component.

---

[6]Note that the lower end of this range is consistent with the column density derived from the H I data for the deep, narrow component of $\sim$3 $\times 10^{20}$ cm^{-2}, assuming a spin temperature $T_{\text{spin}} = 100$ K.
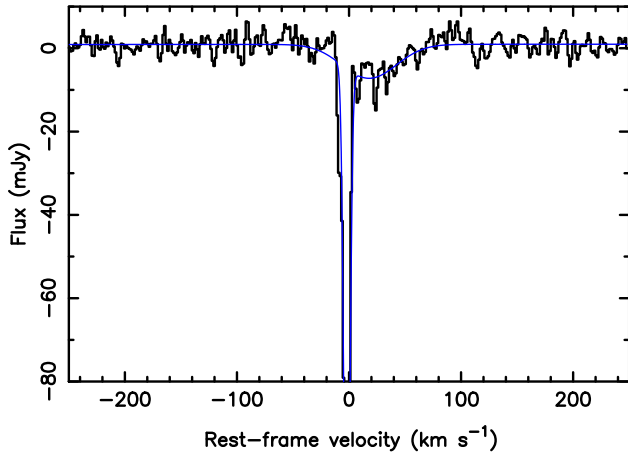
Figure 4. CO absorption profile extracted at the location of the peak continuum of PKS1814–63 (black line), compared with a double-Gaussian fit to the profile (blue line). The profile has been obtained from the cube made at full velocity resolution ($1.4 \, \mathrm{km \, s^{-1}}$) in order to minimize the presence of emission, and the continuum emission has been subtracted. Note that the full depth of the narrow absorption is not shown in order to highlight the shallow, broad feature.

Intriguingly, the shape of the CO(1-0) absorption profile is similar (but not identical) to that of the H I absorption profile (Morganti et al. 2011), which shows both deep (narrow) and shallow (broad) absorption features. However, the broad component seen in CO is less broad than observed in H I (FHWM$_{H_I}$ > $100 \, \mathrm{km \, s^{-1}}$) and, unlike the H I, is only redshifted. This could result from differences in the structure of the extended continuum emission at the two (very different) frequencies: at 1.4 GHz the source consists of two lobes with a total extent of about 400 mas, (~480 pc: Tzioumis et al. 2002), but the diffuse southern lobe (associated with blueshifted H I broad absorption) is fainter and has a steeper spectral index than the northern lobe (associated with redshifted H I broad absorption), so is probably too faint to contribute significant flux at the frequency of our ALMA observations. Therefore, the broad, redshifted CO(1-0) absorption is most likely observed against the northern lobe, which is relatively compact (< 120 pc, see Morganti et al. 2011).

Absorption by molecular gas has also been seen in other radio galaxies (see e.g. Maccagni et al. 2018; Rose et al. 2019, 2024; Ruffa et al. 2019a; Morganti et al. 2021, for some recent examples). In particular, the CO(1-0) absorption detected in Hydra A by Rose et al. (2019, 2020), has a profile that is strikingly similar to that of PKS1814-63, with both broad and narrow components detected, and similar velocity widths and velocity shift amplitudes.

From their study of the CO(1-0) absorption detected against the radio cores of a sample of nearby massive galaxies, Rose et al. (2024) suggest that the absorption profiles indicate the presence of two distinct populations of molecular clouds: on the one hand, clouds with low-velocity dispersion, likely belonging to a galaxy-scale, edge-on disc of molecular gas; on the other, clouds with high-velocity dispersion located in circumnuclear discs and/or tracing bulk movement of molecular gas towards the galaxy centre.

A similar situation may be present in PKS1814-63: Morganti et al. (2011) suggest that the broader HI absorption (which, as described above, shows both red and blue wings) is due to gas located in a circumnuclear disc moving under gravity, with perhaps some of the line width accounted for by projection effects. However, given the relatively large velocity width (FWHM $\sim 60 \, \mathrm{km \, s^{-1}}$) of the broad

CO absorption and the fact that it is seen against such a compact lobe, an alternative possibility is that the large width results from interaction between the gas and the expanding radio jet.

We further note that the similarities between the CO and H I absorption profiles, also highlighted by Rose et al. (2019) for Hydra A, suggest that the H I and the molecular gas may be spatially coincident. This is consistent with the hypothesis that, when heated, cold molecular gas regions produce an encompassing skin of warm atomic gas (e.g. Jaffe, Bremer & Baker 2005).

4.3 Structure and kinematics of the molecular gas

In the detected targets, we find that the molecular gas is distributed over large, extended structures. We measure the diameters of the structures from the lower contour of the total intensity images, and check them using PV diagrams. The estimated full sizes (diameters) are between 4.5 and 25 kpc (see Table 2). These structures are larger than those typically found in nearby low-power radio galaxies and ETG (see Section 5), but similar to the extents of the molecular gas found in radio AGN in rich cluster environments.

In at least five of the detected targets (Hydra A [PKS0915–11], PKS1733–56, PKS1814–63, PKS1949+02, and PKS2314+03), most of the molecular gas appears distributed in discs/rings with relatively regular kinematics (see Fig. A1). It is worth noting that Hydra A represents a rare case of a molecular gas disc found in a cool–core cluster (Rose et al. 2019; Russell et al. 2019). In the case of PKS2314+03 (3C 459), the disc is more clearly seen in the high-resolution data available from the archive (see Section 3). However, tails or clouds of unsettled gas are observed in the outer parts of the distribution of molecular gas in all these objects.

We have investigated the molecular gas kinematics in more detail by modelling the CO using the 3D-Based Analysis of Rotating Object via Line Observations (3D-Barolo), a tool for fitting 3D tilted-ring models to emission-line data cubes, described in Di Teodoro & Fraternali (2015). The main purpose of this modelling was to determine whether rotational motions in a disc or ring provide a good description of the measured gas kinematics.

For this analysis, we concentrated on the four cases where the distribution of the gas is seen to be clearly extended over several beams. The plots resulting from the modelling are shown in Fig. A4, and Table 3 presents the parameters. Given the quality of the data, we fixed as many parameters as possible in the fitting. In particular, the position angle (PA) and inclination used in the fitting were taken from available information like the presence of dust-lanes (see e.g. Ramos Almeida et al. 2011). The velocity dispersion was set to $10 \, \mathrm{km \, s^{-1}}$, but the rotation velocity was always left free in the fitting. The plots in Fig. A4 show that the models describe to first order the data for all the targets, confirming that most of the CO is observed in a regularly rotating structure. However, the plots also show that the limited sensitivity of the observations does not allow a detailed comparison between data and models.

The estimated PAs of the major axes of the discs are compared with the PAs of the (projected) radio axes in Table 3. Since we do not know the orientation of the jet relative to the line of sight, we cannot derive precise values for the de-projected angle of the radio axis relative to the plane of the disc. However, comparing the projected jet and disc PAs, it clear that in a significant number of cases the jet is not perpendicular to the gas disc (see also Fig. A1 where the directions of the radio axes are compared with those of the major axes of the gas discs). We note that this is similar to the situation found in a number of objects studied in literature (e.g. Morganti et al. 2015; Ruffa et al. 2019a, and references therein).

Table 3. Parameters from the modelling of the CO cube with 3D-Barolo, see text for details.

	V_{rot}^a (km s^{-1})	PA^b (°)	Inclination (°)	V_{sys} (km s^{-1})	PA radio (°)	ΔPA^c (projected) (°)	Notes
PKS1733–56	343	–54	+70	80	+38	91	CO aligned with dust-lane
PKS1814–63	245	–51	+74	–3	+7	58	CO aligned with dust-lane
PKS1949+02	327	–135	+53	–165	+80	35	Aligned with dust-lane?
PKS2314+03	247	–75	+75	–60	+90	15	Disturbed galaxy, optical halo/fans
PKS0915-11		–80			+10	90	From Rose et al. (2019)

^{a}From the outer ring. ^{b}Angle of the approaching side. $^c\Delta$PA $= |$ PA$_{CO}$ − PA$_{jet}|$. *Notes.* The second column gives the de-projected rotation velocity, the third column the PA of the major axis of the disc, the fourth column the inclination of the disc rotation axis relative to the line of sight, the fifth column the difference between the systemic velocity of the disc and the galaxy rest frame defined by the redshift, the sixth column the radio axis PA, and the seventh column the difference between the disc and radio axis PAs. The gas velocity dispersion assumed was 10 km s^{-1}. For Hydra A, we list only the PAs of the molecular disc (from Rose et al. 2019) and of the radio jet.

In the case of PKS0806–10, the molecular gas structure is only marginally resolved, so we cannot perform a meaningful modelling. However, the velocity map and PV diagram for this source (see Fig. A1) suggest that at least part of the molecular gas is distributed in a rotating structure and, like some of the objects modelled with 3D-Barolo, in projection the radio axis appears to be aligned close to the major axis of the disc, rather than perpendicular to it.

In two cases – PKS2211–17 (only marginally resolved) and PKS1648+05 – we do not detect velocity gradients across the distribution of CO(1-0) that are suggestive of orderly rotation. Interestingly, both of these radio AGN are located at the centres of galaxy clusters (Croston et al. 2011; Ramos Almeida et al. 2013; Ineson et al. 2015), and the apparent lack of evidence for regular rotation in a disc is consistent with what is typically observed for the molecular gas associated with central cluster galaxies (e.g. McNamara et al. 2014; Olivares et al. 2019) – see Section 6.1 for further discussion.

It is also notable that the CO emission in PKS1932-46 has a highly asymmetric distribution, with all the detected molecular gas located to the north of the nucleus, where it is redshifted by up to ∼200 km s^{-1} relative to the host galaxy rest frame (see Fig. A1). Interestingly, this emission is extended roughly in the direction of a morphologically disturbed, gas-rich companion galaxy at a similar redshift to PKS1932-46 and situated ∼100 kpc to the NE in projection (see Fig. 1). It is possible in this case that the molecular gas has been accreted in a close encounter between the radio AGN host galaxy and its companion in the past (see also discussion in Inskip et al. 2007).

Another example of a ongoing interaction with a companion galaxy is provided by the case of PKS1934–63, where the host is apparently linked to its companion by a tail of molecular gas, and distribution of the CO emission peaks between the two galaxies (see Fig. 1). The PV plot (Fig. A1) shows that the kinematics of the molecular gas has a gradient, with velocities ranging from the systemic velocity of PKS1934–63 to that – about 250 km s^{-1} redshifted – of the companion (see figs 14 and 17 in Roche et al. 2016). Interestingly, the PKS1934–63 (Santoro et al. 2018) is a young radio source that consists of two lobes separated by about 130 pc, and with an estimated kinematic age of ∼10^3 yr (derived by monitoring the lobe separation, Ojha et al. 2004). This close interaction and the presence of molecular gas is particularly interesting in terms of understanding the triggering of the young radio AGN, but much higher spatial resolution observations will be required to investigate this further.

Although we detect some molecular gas with disturbed kinematics, we do not detect fast molecular outflows in CO(1-0) emission in any of our targets. This is likely due to a combination of the relatively shallow depth and limited spatial resolution of the present observations. Molecular outflows in radio AGN have so far been found mainly in young radio sources (Oosterloo et al. 2017, 2019; Murthy et al. 2022; Holden et al. 2024), and their detection has required deep observations combined with high spatial resolution in order to disentangle the outflow from the rest of the molecular gas (which may not be regularly rotating either, e.g. Murthy et al. 2022). Interestingly, we do not find signatures of extreme outflows even in the galaxies that host luminous, quasar-like AGN in addition to the powerful radio jets.

5 COMPARISON WITH OTHER SAMPLES

In order to put our results in a broader context, we now compare them with those obtained for other samples of radio galaxies, nearby quasar-like AGN, and quiescent ETG observed in CO for which statistics have been derived for the occurrence of molecular gas.

5.1 Samples of radio AGN

Details of the main molecular gas studies of samples of radio AGN are summarized in Table 4. The comparison is, of course, limited by differences in the depth and spatial resolution of the various observations, as well as the redshift ranges of the samples studied.

At first sight, it may seem surprising that all the pre-ALMA studies of samples of radio AGN (Evans et al. 2005; Ocaña Flaquer et al. 2010; Smolčić & Riechers 2011) achieve CO detection rates that are comparable with, or significantly higher than, that achieved in this study, despite that fact that their rms sensitivities are a factor of ∼3–100 lower. However, the samples for these studies have median redshifts that are significantly lower ($z < 0.05$) than that of the 2Jy sample used here. This point is further emphasized by the Ruffa et al. (2019a) ALMA interferometric study that has a similar rms sensitivity to that of our 2Jy survey,[7] but targets much lower redshift objects ($z < 0.03$, as illustrated in Fig. 2), and achieves a detection rate that is more than a factor of 2 higher (66 versus 34 per cent), albeit with a small sample.

In addition, the samples used for the pre-ALMA studies are often heterogeneous, incomplete or selected using criteria that may favour

[7]Note, however, that the Ruffa et al. (2019a) observations were made using CO(2-1) rather than CO(1-0).

Table 4. Comparison of CO studies of molecular gas in samples of radio AGN, nearby ETG, and radio-quiet quasars.

Study	N	Redshift range (z)	rms (mJy b^{-1})	Detection rate (per cent)	Selection
Radio AGN pre-ALMA					
Evans et al. (2005)	33	0.02–0.15	7–17	27±8	Detected by *IRAS* (3C, 4C, PKS, B2)
Ocaña Flaquer et al. (2010)	52	< 0.077	1.0–1.7	52±7	$P_{1.4\,GHz} > 10^{22.5}$ W Hz^{-1} (3C, B2, NGC)
Smolčić & Riechers (2011)	21	< 0.1	2.1–5.1	62±11	Type 2 radio AGN observed in X-ray (mainly 3C)
Radio AGN ALMA					
Ruffa et al. (2019a)	9	< 0.03	0.13–0.58	66±16	Volume and flux limited ($S_{2.7\,GHz} > 0.25$ Jy), ETG
Current study	29	0.05–0.3	0.13–0.35	34±9	Complete 2Jy sample, $S_{2.7\,GHz} > 2$ Jy, $\delta < 10°$
Nearby ETG					
Young et al. (2011)	259	< 0.01	6.5–20	22±3	ETG from ATLAS^{3D} sample
Davis et al. (2019)	67	< 0.025	3.4–10	25±5	ETG with $M_* > 10^{11.5}$ M$_\odot$ from MASSIVE sample
Quasar-like AGN ALMA					
Shangguan et al. (2020)	23	< 0.1	1.1–1.7	91±6	PG quasars, radio-quiet
Ramos Almeida et al. (2022)	7	< 0.14	0.12–0.27	71±17	Type 2 quasars, radio-quiet
Molyneux et al. (2024)	17	< 0.2	1.7–4.4	82±9	Type 2 quasars, radio-quiet

Notes. Note that, for the sake of comparison, the rms sensitivities in column 4 have been calculated for a 100 km s^{-1} spectral channel in all cases.

CO detection. For example, Evans et al. (2005) studied radio AGN that were detected by the *IRAS* far-IR satellite. Since the overall detection rate of radio AGN in the *IRAS* survey was low, this selection automatically favours objects with larger than average masses of cool, CO-emitting ISM.

One further factor to consider is the dependence on the host galaxy morphology. In a recent study of a small sample of seven type 2 quasars, Ramos Almeida et al. (2022) found an high detection rate of molecular gas (71±17 per cent). However, all the detections are associated with disc and strongly merging systems, while the two ETG in the sample are undetected in CO. Similar results were found by Husemann et al. (2017) for a sample of nearby type 1 quasar-like objects. This suggests that care should be taken in the comparison of samples of objects in which the galaxies have different morphological types. This has been already seen in the studies of the other cold phase of the gas, i.e. H I see Serra et al. (2012).

5.2 Quiescent ETG samples

We can also expand the comparison to samples of non-active ETG. This is particularly useful for determining whether the molecular properties of the ETG hosts of radio AGN are different from their quiescent counterparts, which might provide clues on how they are triggered.

One of the first systematic molecular CO studies of ETG was performed by Wiklind, Combes & Henkel (1995) using IRAM and SEST. Given the selection of far-IR detected ETG galaxies, the reported (high) CO detection rate (~55 per cent) cannot be considered representative of this group of galaxies. Indeed, later observations of a representative sample 43 galaxies from the SAURON survey of nearby ETG that were not selected on the basis of of their far-IR emission had a lower CO detection rate (28 per cent: Combes, Young & Bureau 2007).

More recent observations of molecular gas in larger samples of ETG were reported for the ATLAS^{3D} sample by Young et al. (2011) and Alatalo et al. (2013), and for the MASSIVE sample by Davis et al. (2019). These samples can be use as reference point for the properties of molecular gas in massive galaxies without strong AGN. However, they focus on objects at much lower redshifts than our 2Jy sample – up to a distance of 107 Mpc ($z \sim 0.025$). In that sense,

they are similar to the sample of radio AGN presented by Ruffa et al. (2019a). While the stellar masses of the ATLAS^{3D} sample objects are lower on average than those of the 2Jy sample, with median of $\sim 3 \times 10^{10}$ M$_\odot$, the MASSIVE sample covers higher stellar masses ($M_* > 3 \times 10^{11}$ M$_\odot$).

Young et al. (2011) found a CO detection rate of 56/259 or 22±3 per cent for the ATLAS^{3D} sample (observed with IRAM-30m) over a range of molecular mass $10^7 < M_{H_2} < 10^{9.2}$ M$_\odot$. For the MASSIVE sample a similar detection rate of CO was found (25±5 per cent), with the molecular masses of the detected sources in the range $10^{8.5} < M_{H_2} < 10^{9.5}$ M$_\odot$. No dependence on the stellar masses of the host galaxy was found, confirming that stellar mass-loss is not the dominant source of the H$_2$ gas in ETG, but rather that (at least a large fraction of) the molecular gas is likely to have an external origin (see Davis et al. 2019 for an overview).

The total CO detection fractions for the ETG samples are similar to the 34±9 per cent we find for the 2Jy sample. However, if we consider the proportion of ETG that have molecular gas masses comparable to those we find for the 2Jy sample (i.e. $\geq 10^{8.9}$ M$_\odot$), large differences are seen: only 1.2±0.7 per cent of the ATLAS^{3D} and 9±3 per cent of the MASSIVE ETG, respectively, have molecular gas masses comparable with those of the detected 2Jy objects[8]; clearly, the hosts of a significant proportion of the 2Jy radio AGN sample are unusually gas-rich compared with the majority of quiescent ETG.

Follow-up observations of ATLAS^{3D} CO detected sources with CARMA interferometer (with a few arcsec resolution, Alatalo et al. 2013), and of small samples of massive ETGs from the WISDOM and MASSIVE samples observed using ALMA (Williams et al. 2023; Dominiak et al. 2024), show that in the majority of the cases the molecular gas is distributed in kinematically settled structures (discs, rings, etc.). These structures have diameters in the range 0.25–10 kpc[9]; however, 24/30 or 80±7 per cent of the ATLAS^{3D}

---

[8]Note that, for the sake of this comparison, we have re-calculated the molecular gas masses from the ATLAS^{3D} and MASSIVE ETG samples using $X_{CO} = 2 \times 10^{20}$ cm^{-2}(K km s^{-1})$^{-1}$ to be consistent with our calculations for the 2Jy sources.

[9]Similar to the technique we have used for the 2Jy objects, here we have estimated the diameters of the molecular discs in the ETG from the lowest contours visible in the maps presented in the relevant papers.

sample in Alatalo et al. ([2013](#)) have molecular disc diameters less than 5 kpc, and the median diameter for the whole sample is 3.6 kpc. Similarly, all nine of the ETGs from the Williams et al. ([2023](#)) and Dominiak et al. ([2024](#)) studies that were not already included in the study of Alatalo et al. ([2013](#)), have molecular disc diameters smaller than 5 kpc, and the median disc diameter is 1.6 kpc. For these samples, the dynamically unsettled cases are only mildly disrupted. Since the detected CO structures are rather compact spatially, with a average radial extent of $\sim$0.8–1.8 kpc, they have correspondingly small dynamical time-scales ($\sim 10^7$–2×10^8 yr) . The molecular gas structures are thus expected to relax and reach equilibrium rapidly.

In comparison, the molecular structures that we detect in the 2Jy radio AGN are notably more extended, with diameters covering the range 4.5–25 kpc (median 13.5 kpc). On the other hand, the properties of the molecular discs detected in lower radio- and optical-luminosity radio AGN by Ruffa et al. ([2019a](#)) are closer to those of the ETG samples: disc diameters in the range 0.4–15 kpc (median $\sim$2 kpc), and only one object – NGC 612[10] – has a diameter greater than 5 kpc.

5.3 Local radio-quiet quasar samples

In order to determine whether there is any difference between the molecular gas reservoirs of nearby radio-loud and radio-quiet AGN, we also compare our results with those for samples of the PG type 1 quasars from Shangguan et al. ([2020](#)) and the type 2 quasars from Ramos Almeida et al. ([2022](#)) and Molyneux et al. ([2024](#)), which are at similar redshifts to the 2Jy sample. Whereas the type 1 quasars in the Shangguan et al. ([2020](#)) cover a similar range of [O III] emission-line luminosity to the SLRG in the 2Jy sample (see Fig. [3](#)), the type 2 quasars have [O III] luminosities at the upper end of the range for the 2Jy SLRG. Both the type 1 and the type 2 quasar samples are dominated by radio-quiet AGN with $P_{1.4\,\mathrm{GHz}} < 10^{24.5}$ W Hz^{-1}.

It is striking that all three of the radio-quiet quasar samples have higher CO detection fractions (71–91 per cent) than the 2Jy sample; however, it is important to be cautious when making this comparison because the quasar observations have different rms sensitivities to that of this study, and the Shangguan et al. ([2020](#)) and Ramos Almeida et al. ([2022](#)) observations targeted the CO(2-1) line rather than the CO(1-0) line. Therefore, we concentrate on comparing the molecular gas masses. We find that 65 ± 10 per cent of the 23 type 1 quasars in Shangguan et al. ([2020](#)), and 90 ± 7 per cent of the 20 type 2 quasars in the sample obtained by combining the those of Ramos Almeida et al. ([2022](#)) and Molyneux et al. ([2024](#)), have molecular gas masses comparable to or greater than those of the detected 2Jy sources ($M_{H_2} \geq 10^{8.9}$ M$_\odot$). For comparison, the detection rate of CO for the 19 SLRG in the 2Jy sample – the radio AGN most comparable with the quasar samples in terms of [O III] luminosity – is only 37 ± 12 per cent. This provides evidence that the host galaxies of local radio-quiet quasars, and in particular local type 2 quasars, are more gas-rich on average than the 2Jy SLRG. However, some of this apparent contrast may be due to differences in host galaxy morphologies (see discussion in Section [5.1](#)). Certainly, the type 1 quasar sample of Shangguan et al. ([2020](#)) has a much higher proportion of disc galaxies (>62 per cent) than the 2Jy radio AGN sample considered in this paper (3 per cent). On the other hand, the proportion of disc galaxies in the full QSOFEED sample of nearby ($z < 0.14$) type 2 quasars – which has higher [O III] luminosities on

average than the Shangguan et al. ([2020](#)) type 1 quasar sample – is relatively low (<21 per cent: Pierce et al. [2023](#)).

6 DISCUSSION

Here, we connect the detection rate, distribution and kinematics of the molecular gas with the properties of the AGN, radio sources and their host galaxies.

6.1 Occurrence, morphology, and origin of the molecular gas

We have detected large amounts of molecular gas in 10 of our targets. For these objects, the mass of the detected H_2 ranges between 8×10^8 and 2×10^{10} M$_\odot$. The upper limits to the H_2 masses from our observations are in the range $\sim 7 \times 10^7$ to a few 10^9 M$_\odot$, and strongly redshift-dependent, as shown in Fig. [2](#). This results in a detection rate – for these high molecular gas masses – of 34 ± 9 per cent.

One point of interest is whether the detection rate of molecular gas depends on the optical spectroscopic and radio morphological classifications of the AGN, perhaps related to different triggering/fuelling mechanisms. Considering first the radio morphology, we find that 1/6 (17 ± 15 per cent) of the FRI and 9/23 (39 ± 10 per cent) of the FRII sources in our sample have CO(1-0) detections. While this difference is consistent with the idea that the two groups are triggered in different ways, for example, FRII sources by mergers and FRI sources by hot gas accretion, the result has a low statistical significance due to the small sample sizes. Moreover, when we consider the optical spectroscopic classifications, we find no evidence for significant differences in the detection rates that might be related to different accretion modes (e.g. Smolčić & Riechers [2011](#)): 3/10 (30 ± 14 per cent) of the WLRG and 7/19 (37 ± 11 per cent) SLRG have molecular detections.

As already noted, in terms of the spatial distribution of molecular gas, where we detect CO emission in the 2Jy objects, it tends to be more extended and show a more irregular structure than found in the spatially resolved studies of lower luminosity (mainly FRI) radio AGN by Ruffa et al. ([2019a](#)) and nearby ETG by Alatalo et al. ([2013](#)), Williams et al. ([2023](#)), and Dominiak et al. ([2024](#)).

At first sight, the relatively large extents and irregular distributions of the molecular gas appear similar to those found in CO observations of cool–core clusters (e.g. Tamhane et al. [2022](#); Russell et al. [2019](#), and references therein). However, the majority of the detected 2Jy sources show a higher degree of rotation in the extended molecular gas than observed in most cool core clusters, and number-count and X-ray studies suggest that most of these objects are also in relatively low-density, group-like environments, rather than clusters (see Table [1](#); Ramos Almeida et al. [2013](#); Ineson et al. [2015](#)). Therefore, it seems unlikely that the molecular gas has condensed from the hot X-ray haloes in such cases, and a galaxy-merger or interaction origin – which could also explain the extent and irregular distribution of the molecular gas – is more plausible.

Although the majority of the detected 2Jy sources are in relatively low-density group-like environments, a minority – comprising PKS0915–11 (Hydra A), PKS1648+05 (Hercules A), and PKS2211–17 – are at the centres of galaxy clusters based on number count analysis and X-ray observations (Ramos Almeida et al. [2013](#); Ineson et al. [2015](#)). Two of them (PKS1648+05, PKS2211–17) show a lack of clear evidence for rotation in the molecular gas, while the third (PKS0915–11) shows a regularly rotating disc with a diameter of 4.5 kpc (Rose et al. [2019](#)). Certainly, for the former two cases, cooling from the X-ray haloes is a plausible alternative to galaxy mergers/interactions as an origin for the molecular gas. Indeed,

---

[10]Interestingly, this is also the only FRII source in the Ruffa et al. ([2019a](#)) sample to be detected in CO.

although they both show evidence for patchy dust absorption in optical images (Ramos Almeida et al. 2011), neither object shows tidal features suggestive of galaxy interactions. On the other hand, of the eight objects in our sample that are in relatively rich, cluster-like environments (see Table 1) – all WLRG and many with tight upper limits on their molecular gas masses – only 38±17 per cent are detected in CO(1-0). This is similar to the CO(1-0) detection rate for the sample as a whole.

We also caution that using the kinematics and distribution of the molecular gas is not a foolproof method for distinguishing a cooling-flow origin. This is illustrated by the case of higher redshift 2Jy object PKS0023–26 ($z = 0.32$), which shows a massive reservoir of molecular gas ($M_{H_2} = 3.1 \times 10^{10}\,M_\odot$) that is extended over a region with diameter 24 kpc and has an irregular distribution, with no clear sign of regular rotation (Morganti et al. 2021). Despite the similarities with the molecular gas properties of cool core clusters, X-ray observations reveal a relatively low X-ray luminosity ($L_{2-10\,keV} < 3 \times 10^{43}\,erg\,s^{-1}$) for this source that is inconsistent with the object being in a rich cluster; rather, the observations are more consistent with interactions in a galaxy group as the most plausible origin for the molecular gas.

Overall, our results suggest that accretion via galaxy interactions is the origin of the molecular gas for the SLRG objects in our sample. Indeed, all the CO-detected SLRG show tidal features in deep optical images that are suggestive of merger events in the recent past (Ramos Almeida et al. 2011). However, while two of the sources have large molecular gas masses ($\sim 10^{10}\,M_\odot$) that are comparable with those of ULIRG-like major gas-rich mergers (e.g. Solomon et al. 1997), most have much lower molecular masses, suggesting that more minor or less-gas-rich mergers play an important role in the triggering of this type of AGN, consistent with the dust mass results (Tadhunter et al. 2014; Bernhard et al. 2022).

We further note that the one CO-detected FRI source in our sample – PKS0915–11 (Hydra A) – has the most compact and regular CO structure ($D \sim 4.5$ kpc, Rose et al. 2019) of all the objects in our sample, despite being in a cluster, and its molecular gas disc is close to perpendicular in projection to its radio axis. All the other CO-detected sources have an FRII or similar radio morphology, and more extended and irregular gas distributions. This is consistent with the *HST* optical imaging study of 3C radio galaxies by de Koff et al. (2000), who found that the detected dust absorption features (dust lanes, patches) are less regular, more extended, on average, and show less evidence for alignment perpendicular to the radio axes in FRII than FRI radio galaxies in their sample. Potentially, it is also consistent with the recent finding by Balmaverde et al. (2022) that FRII galaxies show 'superdisc' structures in ionized gas that are much larger than the compact emission-line structures seen in the FRI sources in their sample of 3CR radio galaxies.

6.2 Molecular gas and the evolution of the radio sources

The radio properties provide information on the stage of evolution of the radio sources, allowing us to explore the relationship between this and the molecular gas. In particular, young radio sources can be identified as Peaked Sources (see O'Dea & Saikia (2021) – sometimes labelled as CSS or GPS – and they are often found embedded in a particularly rich medium compared to the large (and more evolved) sources. In the sample studied here, there are three targets classified as CSS/GPS: PKS1151–34, PKS1814–63, PKS1934–63, and a further object – PKS2314+03 – represents an intermediate case of a radio source on galactic scales (diameter ~ 50 kpc) that also has a steep-spectrum radio core. Of these objects,

only PKS1151–34 is not detected in CO(1-0), but it is the highest redshift object in the full sample, and consequently has a relatively high molecular gas mass upper limit ($M_{H2} < 3 \times 10^9\,M_\odot$). All the others are detected, although the fraction of molecular gas associated with PKS1934–63 is unclear at the resolution of the present data.

These findings can be combined with those available in the literature. For example, two more 2Jy radio galaxies classified as CSS/GPS sources have recently been observed and studied in detail with ALMA: PKS1549–79 and PKS0023–26 (see Oosterloo et al. 2019; Morganti et al. 2021). Both show massive molecular gas reservoirs ($M_{H_2} > 10^{10}\,M_\odot$), that would have been readily detected if observed as part of the current survey. Overall, all six of the CSS/GPS and related objects from the wider 2Jy sample of Tadhunter et al. (1998) at redshifts $z < 0.4$ have now been observed with ALMA, and 5 (83±17 per cent) of them are detected in CO. This high rate of detection reinforces the idea that the host galaxies of such sources have a richer cool ISM, on average, than the more common extended radio sources in the same sample, consistent with the fact that they also show higher incidence of recent star formation activity (Morganti et al. 2011; Tadhunter et al. 2011; Dicken et al. 2012).

6.3 Gas-to-dust ratio

The detection of CO emission in our sample objects shows a strong correlation with the detection of dust features (lanes, patches) in existing ground-based optical images. Ramos Almeida et al. (2011) found that 7 of the 29 objects in the 2Jy sample with redshifts in the range $0.05 < z < 0.3$ show certain or possible dust features in Gemini r′-band optical images: PKS0915-11 (Hydra A), PKS1559+02 (3C327), PKS1648+05 (Her A), PKS1733-56, PKS1814-63, PKS1949+02 (3C403), PKS2211-17 (3C444). Of these, all but one – PKS1559 + 02 – are detected in CO(1-0). In contrast, PKS0806–10 and PKS1942–46 were detected in CO(1-0) but show no clear dust features in the optical images.

Given that the detection or not of dust features depends on a number of factors (e.g. dust mass, geometry, orientation, and spatial resolution), the optical images provide only a lower limit on the true rate of occurrence of dust *at some level* in the host galaxies. Indeed, *Spitzer* and *Herschel* observations of our sample reveal the presence of dust in the form of thermal bumps at far-IR wavelengths in several objects for which no dust features were detected in optical images (Dicken et al. 2008, 2023). Based on the far-IR observations, robust dust masses have been estimated by Bernhard et al. (2022) using grey-body fits to the SEDs of the thermal dust emission. The derived dust masses depend to some extent on the assumptions made in making the fits (e.g. the β index[11]), but Bernhard et al. (2022) show that they are likely to be accurate to within a factor of 2. The dust masses presented in Table 2 are those calculated by Bernhard et al. (2022) for the cool dust assuming $\beta = 2$.

In Fig. 5, we show the distribution of gas-to-dust mass ratios as function of the molecular gas mass. These were calculated by simply dividing the molecular gas mass by the dust mass. The gas-to-dust ratios of the detections – with an mean value of $M_{gas}/M_{dust} \sim 90$ – are often below typical Galactic values and those found for disc galaxies and ETG in general ($120 < M_{gas}/M_{dust} < 450$; Li & Draine 2001; Zubko, Dwek & Arendt 2004; Draine et al. 2007; Rémy-Ruyer et al. 2014; De Vis et al. 2019; Casasola et al. 2020), but this likely to be due in part to the fact that we have not accounted for the

---

[11] The β index is the spectral index of the power law that modifies the *Planck* curve black body spectrum for optically thin, grey-body dust emission.
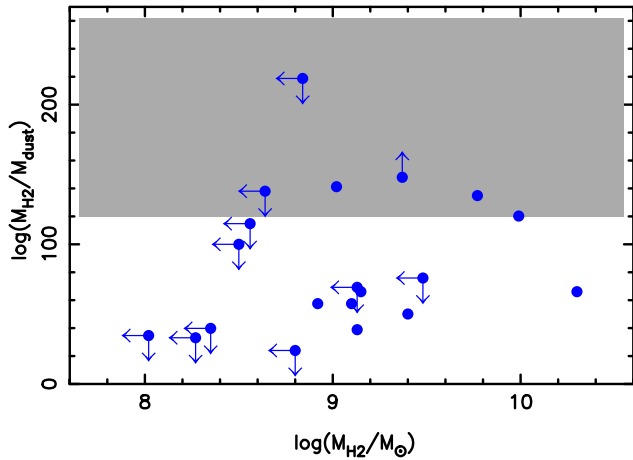
Figure 5. Distribution molecular-gas-to-dust ratio as a function of H_2 mass for the 2Jy sample. Blue-filled circles represent objects detected in both dust and H_2, while blue-filled circles with arrows represent objects with upper or lower limits on the gas-to-dust ratio. Objects that have upper limits in both dust and gas masses are not included. The shaded region represents the lower end of the range of typical total gas-to-dust ratios for disc galaxies.

contribution of neutral HI gas, which could increase the total gas mass by a factor of 2 or more. Furthermore, as expected, most of the CO-detected objects also have dust detections at far-IR wavelengths. The one exception is PKS1932–46, which is detected in CO(1-0) but has an uncertain detection of dust emission at far-IR wavelengths, due to the potential contamination by non-thermal radiation from the core of the radio source, which is relatively strong in our ~100-GHz continuum image, and is also detected by APEX/LABOCA at 870 μm (344 GHz) (Dicken et al. 2023). However, apart from this one object, there are no objects in our sample with high-mass, cool ISM components (detected in CO) that were missed in the *Herschel* observations because of non-thermal contamination, or because of a lack of observations at the longer far-IR wavelengths (> 160 μm) combined with low dust temperatures.

On the other hand, we note that five objects – PKS0806–10, PKS0349–27, PKS0945+07, PKS1559+02, and PKS2221–02 – show notably low values or upper limits for the gas-to-dust ratio: $M_{gas}/M_{dust} < 50$. Of these objects, the case of PKS1559+02 (3C327) is particularly interesting. In many ways, it shows very similar properties to PKS0806–10: redshift $z \sim 0.1$, quasar-like [O III] emission-line and 24 μm continuum luminosities, and relatively high dust mass ($M_{dust} \sim 10^{7.5} M_\odot$). However, unlike PKS0806-10, it is not detected in CO(1-0), and its gas/dust ratio is a factor of ~2× or more lower ($M_{gas}/M_{dust} < 24$). Such low gas-to-dust ratios are rare but not unique. A comparable low value (gas-to-dust ratio = 28) has been reported by Morokuma-Matsui et al. (2019) in the case of Fornax A. One possible explanation in the case of PKS1559+02 is that a massive gas reservoir is present, but is dominated by non-molecular phases of the ISM, such as the cool HI or warm-ionized phases, perhaps as a consequence of the heating and ionizing effect of the quasar-like AGN present in this object.

Aside from physical explanations, an alternative possibility is that the CO emission is significantly more extended than the single ALMA beam we have used to estimate the upper limits on the molecular gas masses (see section 4.1). Certainly, as we have seen, all the CO-detected objects are resolved and cover more than one beam, in some cases several beams. Taking this into account, and also the factor 2 uncertainty in the dust masses, it is possible that the

true gas-to-dust ratios in the apparently discrepant objects are closer to typical Galactic values (i.e. $\gtrsim 100$). However, deeper ALMA observations, that are more sensitive to low surface brightness CO emission that covers several beams, will be required to confirm that the molecular gas reservoirs are truly extended in this way in the so-far undetected sources.

Finally, we should bear in mind that the values we quote are averaged values inside large structures, which do not take into account that the gas-to-dust ratio may change with the locations across the distribution of the molecular gas (e.g. with the distance from the AGN). This has been reported for Cen A by Parkin et al. (2012), who found average a gas-to-dust mass ratio of 103, but with an increase in this ratio to approximately 275 towards the centre of Cen A.

6.4 Molecular gas in radio AGN: the broader galaxy context

Over the last few decades there has been considerable progress in understanding the relationships between properties such as stellar mass, SFR and gas content for the general population of non-active galaxies. For well-resolved nearby galaxies, one of the clearest correlations is found between the surface density of the SFR and that of the gas mass, which encompasses normal disc galaxies as well as starbursts (Schmidt 1959; Kennicutt 1998); however, there are also strong trends between the global (spatially integrated) properties of galaxies. For example, there is a clear correlation between total stellar mass and SFR for star-forming galaxies (the 'main sequence': Noeske et al. 2007), and the total SFR is also found to be correlated with total molecular gas mass for such galaxies (e.g. Saintonge & Catinella 2022). It is important to determine how radio AGN fit in with these global correlations, since this might provide information about the extent to which the jet and AGN activity affect the star formation in the host galaxies – the so-called AGN feedback effect.

In our previous *Herschel*-based work on the 2Jy sample, we found that the majority of radio AGN fall on or below the main sequence for star formation, and from a comparison between the SFRs and gas masses (estimated from dust masses), we deduced that their star formation efficiencies are comparable with, or higher than, those of typical star-forming galaxies (Bernhard et al. 2022). Our ALMA results provide an opportunity to extend these results.

The top panel of Fig. 6 shows SFR plotted against molecular gas mass for the objects in our ALMA study, with the dashed diagonal lines representing molecular gas depletion times – a measure of the star formation efficiency. For comparison, we also show results for local type 1 and type 2 quasars (Jarvis et al. 2020; Shangguan et al. 2020; Ramos Almeida et al. 2022). Consistent with previous results based on *Herschel*-derived dust masses, it clear that the radio AGN have relatively short gas depletion times $t_{dep} \lesssim 10^9$ yr, suggesting high star formation efficiencies. For reference, galaxies on the star-forming main sequence with similar stellar masses to the radio AGN ($\overset{>}{\sim} 10^{11} M_\odot$), have molecular gas depletion times of $t_{dep} \sim 10^9$ yr (Saintonge & Catinella 2022), whereas the discs of nearby normal spiral galaxies have depletion times that are typically longer ($t_{dep} \sim 2 \times 10^9$ yr; Bigiel et al. 2008). Comparing with other AGN, on average, the radio AGN gas depletion times are similar to those of the local quasar samples shown in Fig. 6, and Seyfert galaxies (Salvestrini et al. 2022), but shorter than those of low-luminosity AGN (LLAGN) (Casasola et al. 2015) and the molecular disc of Centaurus A (Espada et al. 2019).

Perhaps the tightest correlation between the gas and stellar properties of galaxies is that between the ratio of molecular gas mass and
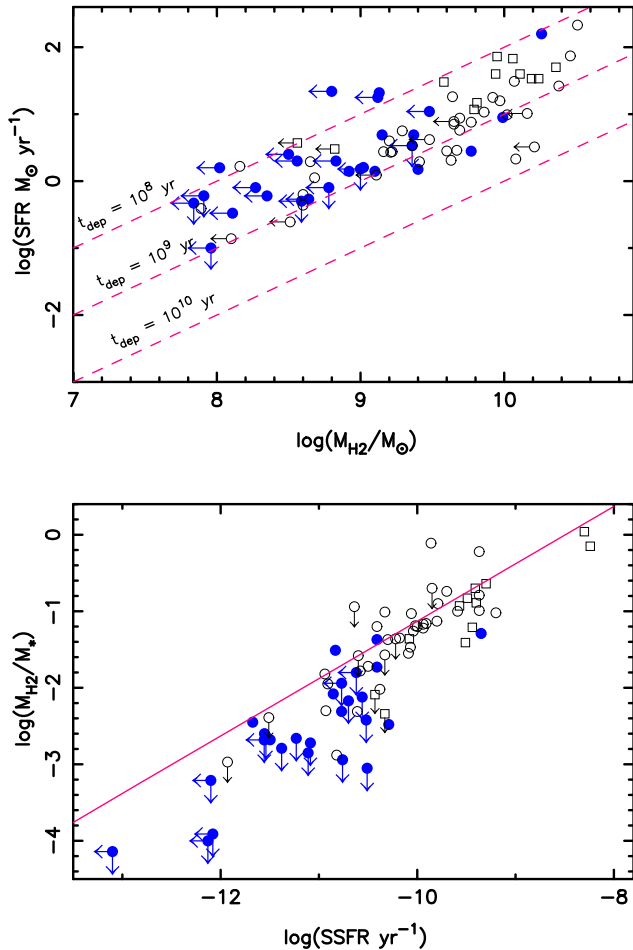
Figure 6. The relationship between stellar mass, molecular gas mass and SFR for the 2Jy radio AGN sample (solid blue symbols). Top panel: SFR versus molecular gas mass, with gas depletion times shown as diagonal-dashed magenta lines. Bottom panel: molecular-to-stellar mass ratio versus specific star formation rate (SSFR), with the correlation derived by (Saintonge & Catinella 2022) for the general galaxy population in the local universe shown as the solid magenta line. To make these plots, we used the stellar masses and SFR for the 2Jy sources derived by Bernhard et al. (2022) following correction for AGN contamination of the far-IR continuum using a template-fitting approach. For comparison, in both plots we also show the results for type 1 quasars (open black circles) from Shangguan et al. (2020), and type 2 quasars (open black squares) with stellar mass estimates from Ramos Almeida et al. (2022) and Jarvis et al. (2020).

stellar mass (i.e. M_{H_2}/M_*) and the SSFR (SSFR = SFR/M_*) (see Saintonge & Catinella 2022, and references therein). The bottom panel of Fig. 6 shows where the radio AGN fall relative this correlation (the solid line represents the general galaxy population). From this, it is clear that both the radio AGN and radio-quiet quasars fall on or below the correlation. This implies that these luminous AGN populations have similar or higher specific SFRs for a given molecular-to-stellar mass ratio compared with the general galaxy population.

Overall, we find no evidence that the SFRs of the radio AGN host galaxies have been reduced compared with what one would expect for non-active galaxies with similar properties; clearly, in these objects, the effects of negative AGN feedback on star formation are not strongly manifested on the time-scales of the AGN activity. This ties in with the idea that the most important impacts of AGN feedback

on galaxy evolution are cumulative – the combined effect of several cycles of AGN activity over long time-scales – rather than clearly detectable in a single activity cycle (see Harrison & Ramos Almeida 2024, and references therein).

7 SUMMARY AND CONCLUSIONS

We have reported the results of an ALMA CO(1-0) survey of the complete sample of 29 2Jy radio AGN with redshifts $0.05 < z < 0.3$. The key results and conclusions are as follows.

(i) The detection rate of CO(1-0) molecular emission for the 2Jy sample (34±9 per cent) is comparable to, or lower than, that of pre-ALMA CO surveys of samples of radio AGN (27–62 per cent), despite the considerably higher sensitivity of the ALMA observations. This apparently surprising result may be explained by the fact that (a) the pre-ALMA surveys covered samples that were at notably lower redshifts on average than the 2Jy sample; (b) with their relatively small beam size (FWHM ~ 2 arcsec) the ALMA observations may have missed diffuse emission on large scales around the host galaxies; (c) as well as any large-scale diffuse emission, the larger beams of the pre-ALMA survey observations (FWHM ~5–20 arcsec) may have admitted emission from nearby companion galaxies in some cases.

(ii) All the early-type host galaxies of the CO-detected 2Jy sources have relatively large masses of molecular hydrogen ($8 \times 10^8 < M_{H_2} < 2 \times 10^{10}\,M_\odot$), and the proportion (34±9 per cent) of the sample showing such large molecular masses is notably higher than for the nearby ATLAS^{3D} and MASSIVE samples of early-type non-active galaxies (1.1 and 9 per cent, respectively: Young et al. 2011; Davis et al. 2019), and the sample of lower luminosity radio AGN observed with ALMA by Ruffa et al. (2019a: 11 per cent).

(iii) Although the detection rate of relatively large molecular gas masses is higher for the 2Jy radio AGN than for samples of nearby ETG, it is lower than those derived for samples of local, radio-quiet quasars observed by ALMA (Shangguan et al. 2020; Ramos Almeida et al. 2022; Molyneux et al. 2024). This suggests that luminous, radio-loud AGN are less gas-rich, on average, than their radio-quiet counterparts.

(iv) The molecular gas in many of the 2Jy objects is distributed in large (4.5–25 kpc diameter), rotating disc structures that show signs of distortion and irregularity in their outer reaches. In contrast, the molecular discs in nearby ETGs, and radio AGN with lower luminosities, tend to be more compact (typical diameters ~2–5 kpc) and show less evidence for significant structural distortion (Alatalo et al. 2013; Ruffa et al. 2019a). Moreover, the molecular discs of the 2Jy objects are not always perpendicular to the radio axes, but show a wide range of projected alignments.

(v) Given the 1–2 orders of magnitude spread in molecular gas masses for a given AGN luminosity, it is unlikely that the mass of the molecular gas reservoir is the sole determinant of the level of AGN activity; other factors (e.g. the degree to which the cold gas is dynamically settled) must also be important.

(vi) At the sensitivity and resolution of our observations we see no evidence for molecular outflows in CO(1-0) emission in any of the detected 2Jy sources. However, one source – PKS1814–63 – shows a relatively broad CO(1-0) absorption component against a compact synchrotron-emitting lobe close to its nucleus. This may be a sign of turbulence induced by the interaction between the radio jets and the circumnuclear ISM.

(vii) The 2Jy radio AGN have relatively small gas depletion times ($t_{dep} \lesssim 10^9$ yr) for their stellar masses ($M_* \gtrsim 10^{11}\,M_\odot$) and fall on, or close to, the correlation between molecular-to-stellar mass ratio

and specific SFR found for the general non-active galaxy population. Therefore, there is no evidence that negative AGN feedback has affected the star formation efficiencies in their host galaxies on the time-scale of the AGN lifecycle.

Together, the high masses, rotational kinematics, large extents, and distorted outer structures of the molecular gas in many of the CO-detected 2Jy objects suggest an external origin for the gas. This is consistent with the results of deep imaging observations, and supports the idea that the powerful AGN and jet activity has been triggered by galaxy interactions, as the accreted gas settles into a stable dynamical configuration. However, a minority of the detected sources situated in relatively rich cluster environments show molecular gas properties that are more akin to those of cool core clusters. In such cases, the accretion of gas that has cooled from the hot X-ray haloes is a plausible alternative to galaxy interactions as a triggering mechanism.

DATA AVAILABILITY

The reduced data underlying this paper will be shared on reasonable request to the corresponding author, and the raw data are publicly available via the ALMA archive.

REFERENCES

Alatalo K. et al., 2013, MNRAS, 432, 1796
Audibert A. et al., 2022, A&A, 668, 67
Audibert A. et al., 2023, A&A, 671, L12
Balmaverde B. et al., 2022, A&A, 662, A23
Bernhard E., Tadhunter C. N., Pierce J. C. S., Dicken D., Mullaney J. R., Morganti R., Ramos Almeida C., Daddi E., 2022, MNRAS, 512, 86
Best P. N., Kaiser C. R., Heckman T. M., Kauffmann G., 2006, MNRAS, 368, L67
Bigiel F., Leroy A., Walter F., Brinks E., De Block W., Madore B., Thornley M., 2008, AJ, 136, 2846
Boizelle B. D. et al., 2021, ApJ, 908, 19
Bolatto A. D., Wolfire M., Leroy A. K., 2013, ARA&A, 51, 207
Bridges T. J., Irwin J. A., 1998, MNRAS, 300, 967
Carilli C. L., Perley R. A., Perley D. A., Dhawan V., Decarli R., Evans A. S., Nyland K., 2022, ApJ, 937, 106
CASA team et al., 2022, Publ. Astron. Soc. Aust., 134, 4501
Casasola V., Hunt L., Combes F., Garcí-Burillo S., 2015, A&A, 577, A135
Casasola V. et al., 2020, A&A, 633, A100
Combes F., Young L. M., Bureau M., 2007, MNRAS, 377, 1795
Croston J. H., Hardcastle M. J., Mingo B., Evans D. A., Dicken D., Morganti R., Tadhunter C. N., 2011, ApJ, 734, L28
Dasyra K. M., Combes F., Novak G. S., Bremer M., Spinoglio L., Pereira S. M., Salomé P., Falgarone E., 2014, A&A, 565, A46
Davis T. A., Greene J. E., Ma C.-P., Blakeslee. J. P., Dawson J. M., Pandya V., Veale M., Zabel N., 2019, MNRAS, 486, 1404
De Vis P. et al., 2019, A&A, 623, A5
de Koff S. et al., 2000, ApJS, 129, 33
Di Teodoro E. M., Fraternali F., 2015, MNRAS, 451, 3021
Dicken D., Tadhunter C., Morganti R., Buchanan C., Oosterloo T., Axon D., 2008, ApJ, 678, 712
Dicken D., Tadhunter C., Axon D., Morganti R., Inskip K. J., Holt J., González Delgado R., Groves B., 2009, ApJ, 694, 268
Dicken D. et al., 2012, ApJ, 745, 172
Dicken D., Tadhunter C. N., Nesvadba N. P. H., Bernhard E., Könyves V., Morganti R., Ramos Almeida C., Oosterloo T., 2023, MNRAS, 519, 5807
Dominiak P., Bureau M., Davis T. A., Ma C-P., Greene J. E., Gu M., 2024, MNRAS, 529, 1597
Draine B. T. et al., 2007, ApJ, 663, 866
Espada D. et al., 2017, ApJ, 843, 136
Espada D. et al., 2019, ApJ, 887, 88
Evans A. S., Mazzarella J. M., Surace J. A., Frayer D. T., Iwasawa K., Sanders D. B., 2005, ApJS, 159, 197
Fabian A., 1999, MNRAS, 308, L39
García-Burillo S. et al., 2021, A&A, 652, A98
Girdhar A. et al., 2022, MNRAS, 512, 1608
Harrison C. M., Costa T., Tadhunter C. N., Flutsch A., Kakkad D., Perna M., Vietri G., 2018, NatAs, 2, 198
Harrison C. M., Ramos Almeida C., 2024, Galaxies, 12, 17
Hamer S. L. et al., 2016, MNRAS, 460, 1758
Hardcastle M. J., Evans D. A., Croston J. H., 2007, MNRAS, 376, 1849
Heckman T. M., Kauffmann G., Brinchmann J., Charlot S., Tremonti C., White S. D. M., 2004, ApJ, 613, 109
Heyer M., Krawczyk C., Duval J., Jackson J. M., 2009, ApJ, 699, 1092
Holden L. R., Tadhunter C., Audibert A., Oosterloo T., Ramos Almeida C., Morganti R., Pereira-Santaella M., Lamperti I., 2024, MNRAS, 530, 446
Holt J., Tadhunter C. N., González Delgado R. M., Inskip K. J., Rodriguez Zaurín J., Emonts B. H. C., Morganti R., Wills K. A., 2007, MNRAS, 381, 611
Holt J., Tadhunter C. N., Morganti R., 2008, MNRAS, 387, 639
Hunter R. H. et al., 2023, Publ. Astron. Soc. Pac., 135, 074501
Husemann B., Davis T. A., Jahnke K., Dannerbauer H., Urrutia T., Hodge J., 2017, MNRAS, 470, 1570
Ineson J., Croston J. H., Hardcastle M. J., Raft R. P., Evans D. A., Jarvis M., 2015, MNRAS, 453, 2682
Inskip K. J., Tadhunter C. N., Dicken D., Holt J., Villar-Martín M., Morganti R., 2007, MNRAS, 382, 95
Jaffe W., Bremer M. N., Baker K., 2005, MNRAS, 360, 748
Jarvis M. E. et al., 2020, MNRAS, 498, 1560
Kennicutt R. C., Jr., 1998, ApJ, 498, 541
King A. R., Pounds K. A., 2015, ARA&A, 53, 115
Koss M. J. et al., 2022, ApJS, 261, 2
Li A., Draine B. T., 2001, ApJ, 554, 778
McNamara B. R., Nulsen P. E. J., 2012, New J. Phys., 14, 055023
McNamara B. R. et al., 2014, ApJ, 785, 44
Maccagni F. M. et al., 2021, A&A, 656, A45
Maccagni F. M., Morganti R., Oosterloo T. A., Oonk J. B. R., Emonts B. H. C., 2018, A&A, 614, A42
Mingo B., Hardcastle M. J., Croston J. H., Dicken D., Evans D. A., Morganti R., Tadhunter C., 2014, MNRAS, 440, 269
Molyneux S. J. et al., 2024, MNRAS, 527, 4420
Morganti R., Killeen N. E. B., Tadhunter C. N., 1993, MNRAS, 263, 1023

Morganti R., Oosterloo T., Tadhunter C., Aiudi R., Jones P., Villar-Martín M., 1999, A&AS, 140, 355

Morganti R., Holt J., Tadhunter C., Ramos Almeida C., Dicken D., Inskip K., Oosterloo T., Tzioumis T., 2011, A&A, 535, A97

Morganti R., Oosterloo T., Oonk J. B. R., Frieswijk W., Tadhunter C., 2015, A&A, 580, A1

Morganti R., Oosterloo T., Tadhunter C., Bernhard E., Oonk R., 2021, A&A, 656, A55

Morokuma-Matsui K. et al., 2019, Publ. Astron. Soc. Japan, 71, 85

Mukherjee D., Bicknell G. V., Sutherland R., Wagner A., 2016, MNRAS, 461, 967

Murthy S., Morganti R., Wagner A. Y., Oosterloo T., Guillard P., Mukherjee D., Bicknell G., 2022, NatAs, 6, 488

Noeske K. G. et al., 2007, ApJ, 660, L43

North E. V. et al., 2019, MNRAS, 490, 319

Ocaña Flaquer B., Leon S., Combes F., Lim J., 2010, A&A, 518, A9

O'Dea C. P., Saikia D. J., 2021, A&A Rev., 29, 3

Ojha R. et al., 2004, AJ, 127, 1977

Olivares V. et al., 2019, A&A, 631, A22

Oosterloo T., Raymond Oonk J. B., Morganti R., Combes F., Dasyra K., Salomé P., Vlahkis N., Tadhunter C., 2017, A&A, 608, A38

Oosterloo T., Morganti R., Tadhunter C., Oonk R., Bignall H. E., Tzioumis T., Reynolds C., 2019, A&A, 632, A66

Oosterloo T., Morganti R., Murthy S., 2024, Nat. Astron., 8, 256

Parkin T. J. et al., 2012, MNRAS, 422, 2291

Pierce J. C. S et al., 2022, MNRAS, 510, 1163

Pierce J. C. S. et al., 2023, MNRAS, 522, 1736

Ramos Almeida C., Tadhunter C. N., Inskip K. J., Morganti R., Holt J., Dicken D., 2011, MNRAS, 410, 1550

Ramos Almeida C., Bessiere P. S., Tadhunter C. N., Inskip K. J., Morganti R., Dicken D., González-Serrano J. I., Holt J., 2013, MNRAS, 436, 997

Ramos Almeida C. et al., 2022, A&A, 658, A155

Rémy-Ruyer A. et al., 2014, A&A, 563, A31

Roche N., Humphrey A., Lagos P., Papaderos P., Silva M., Cardoso J. S. M., Gomes J. M., 2016, MNRAS, 459, 4259

Rose T. et al., 2019, MNRAS, 485, 229

Rose T. et al., 2020, MNRAS, 496, 364

Rose T. et al., 2024, preprint (arXiv:2403.03974)

Ruffa I. et al., 2019a, MNRAS, 484, 4239

Ruffa I. et al., 2019b, MNRAS, 489, 3739

Ruffa I., Laing R. A., Prandoni I., Paladino R., Parma P., Davis T. A., 2020, MNRAS, 499, 5719

Russell H. R. et al., 2019, MNRAS, 490, 3025

Saintonge A., Catinella B., 2022, ARA&A, 60, 319

Salome P., Combes F., 2008, A&A, 489, 101

Salvestrini F. et al., 2022, A&A, 663, A28

Santoro F., Rose M., Morganti R., Tadhunter C., Oosterloo T. A., Holt J., 2018, A&A, 617, A139

Santoro F., Tadhunter C., Baron D., Morganti R., Holt J., 2020, A&A, 644, A54

Schmidt M., 1959, ApJ, 129, 243

Serra P. et al., 2012, MNRAS, 422, 1835

Serra P. et al., 2015, MNRAS, 448, 1922

Shangguan J., Ho L. C., Bauer F. E., Wang R., Treister E., 2020, ApJ, 899, 112

Smolčić V., Riechers D. A., 2011, ApJ, 730, 64

Solomon P. M., Downes D., Radford S. J. E., Barrett J. W., 1997, ApJ, 478, 144

Tadhunter C., 2016, A&A Rev, 24, 10

Tadhunter C. N., Morganti R., di Serego Alighieri S., Fosbury R. A. E., Danziger I. J., 1993, MNRAS, 263, 999

Tadhunter C. N., Morganti R., Robinson A., Dickson R., Villar-Martín M., Fosbury R. A. E., 1998, MNRAS, 298, 1035

Tadhunter C. et al., 2011, MNRAS, 412, 960

Tadhunter C., Dicken D., Morganti R., Konyves V., Ysard N., Nesvadba N., Ramos Almeida C. R., 2014, MNRAS, 445, L51

Tamhane P. D., McNamara B. R., Russell H. R., Edge A. C., Fabian A. C., Nulsen P. E., Babyk I. V., 2022, MNRAS, 516, 861

Tremblay G. R. et al., 2016, Nature, 534, 218

Tzioumis A. et al., 2002, A&A, 392, 841

van Kempen T. A. et al., 2014, ALMA Memo, 599

Veilleux S., Cecil G., Bland-Hawthorn J., 2005, ARA&A, 43, 769

Wiklind T., Combes F., Henkel C., 1995, A&A, 297, 643

Williams T. G. et al., 2023, MNRAS, 525, 4270

Young L. M. et al., 2011, MNRAS, 414, 940.

Zubko V., Dwek E., Arendt R. G., 2004, ApJS, 152, 211

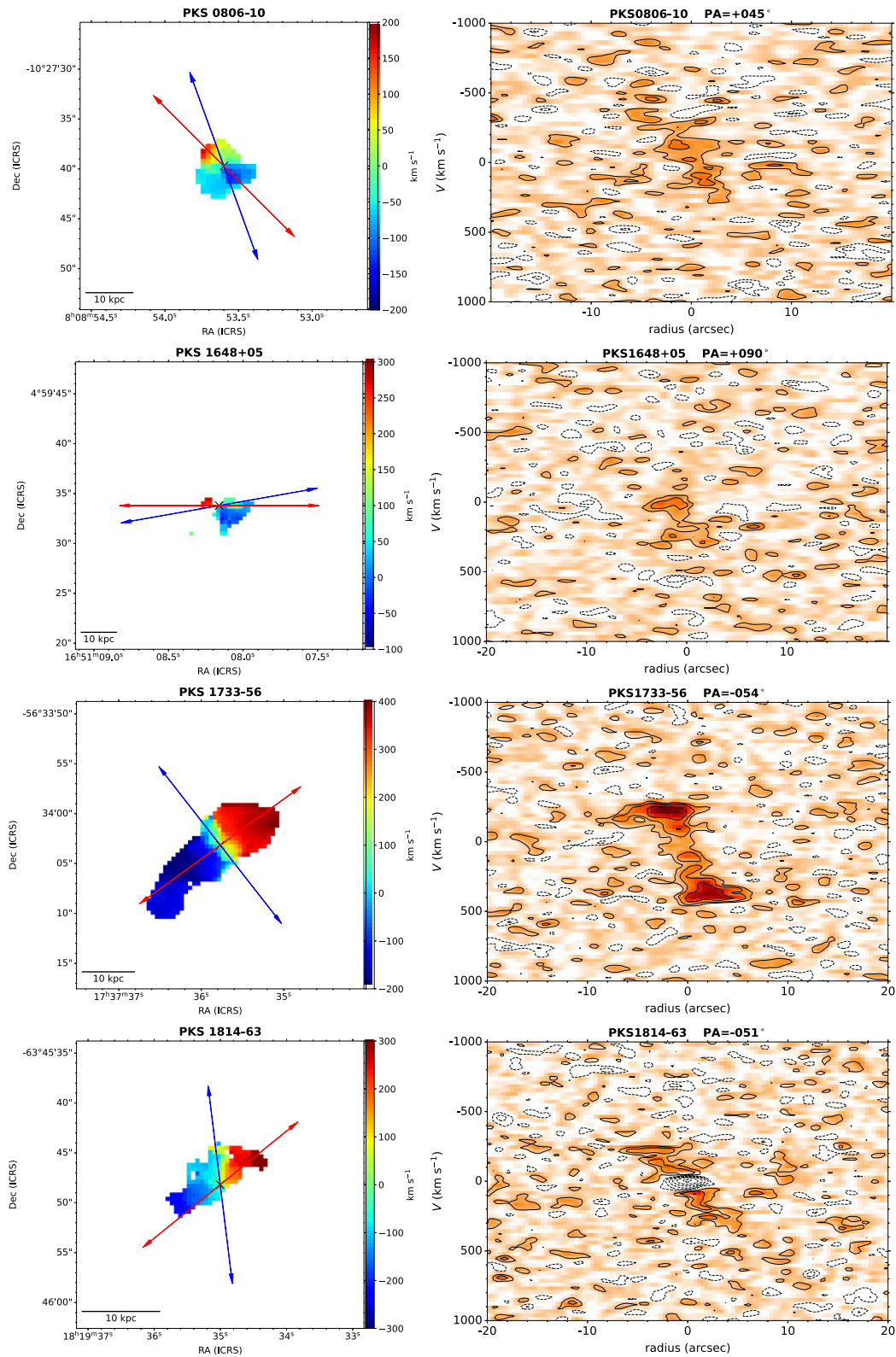# APPENDIX A: ADDITIONAL FIGURES FOR DETECTED SOURCES

Figure A1. Velocity fields of the CO-detected targets (left panel) and PV plots along the major axis of the emission (right panel). The cross indicates the position of the AGN. The blue arrow indicates the direction of the radio jets, whereas the red arrow indicates the major axis PA along which the PV plot was made. Contour levels in the PV plots are –2, 2, 4, 6,...., σ.
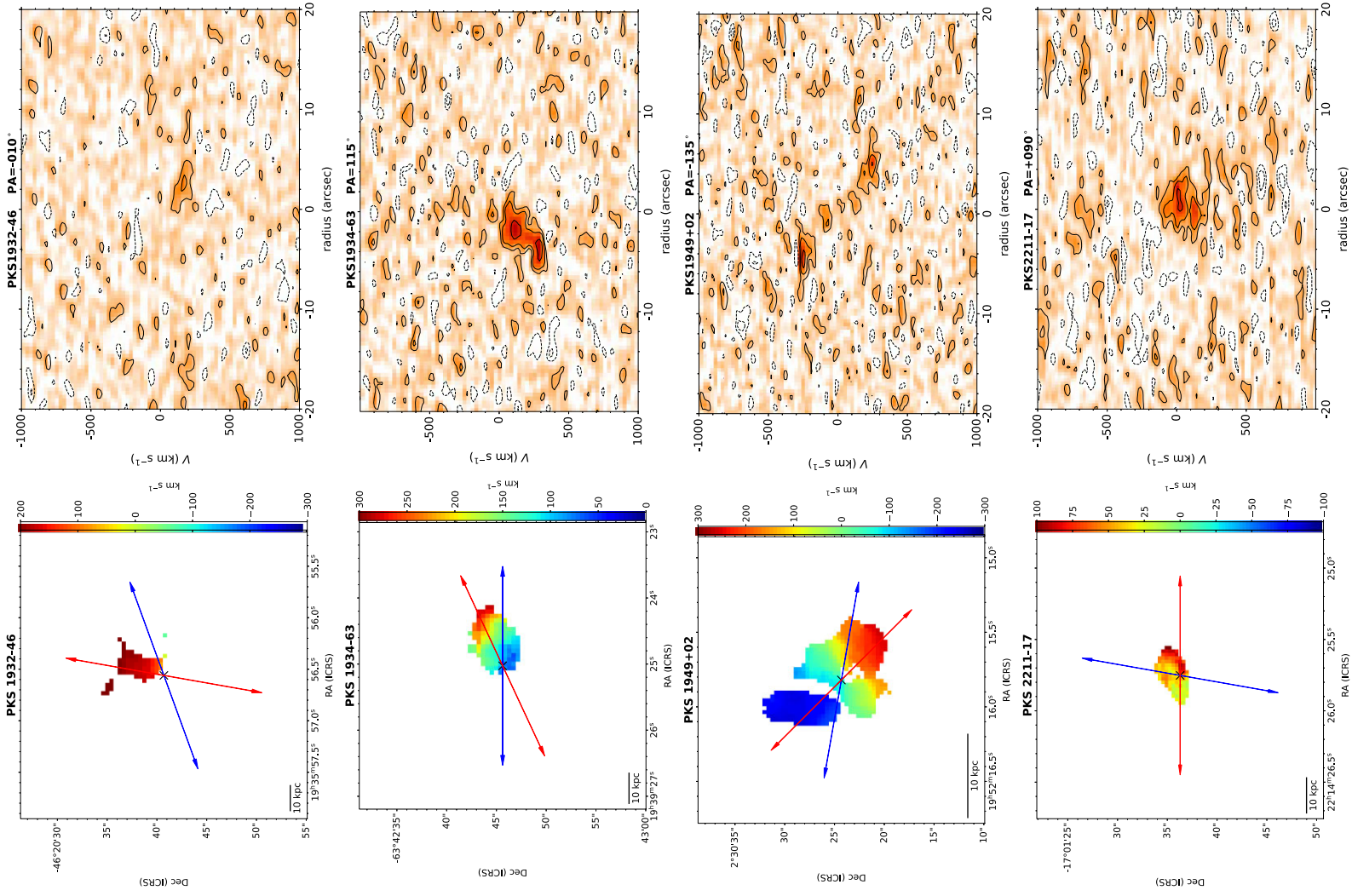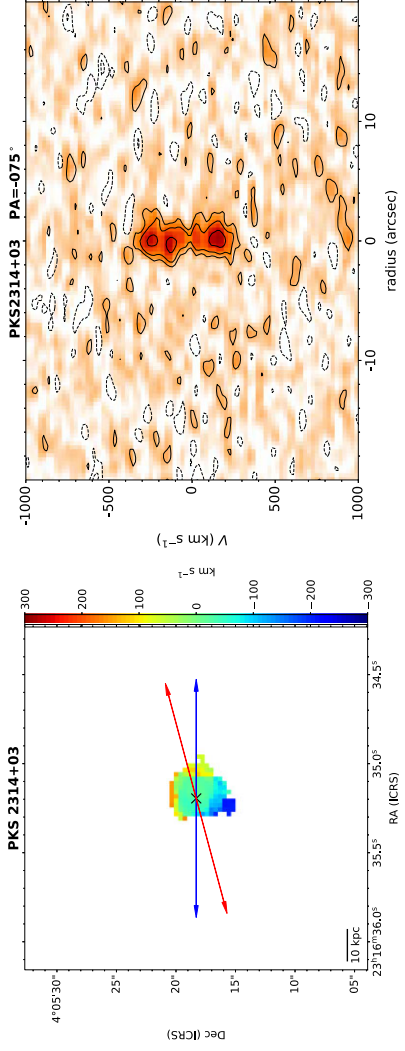
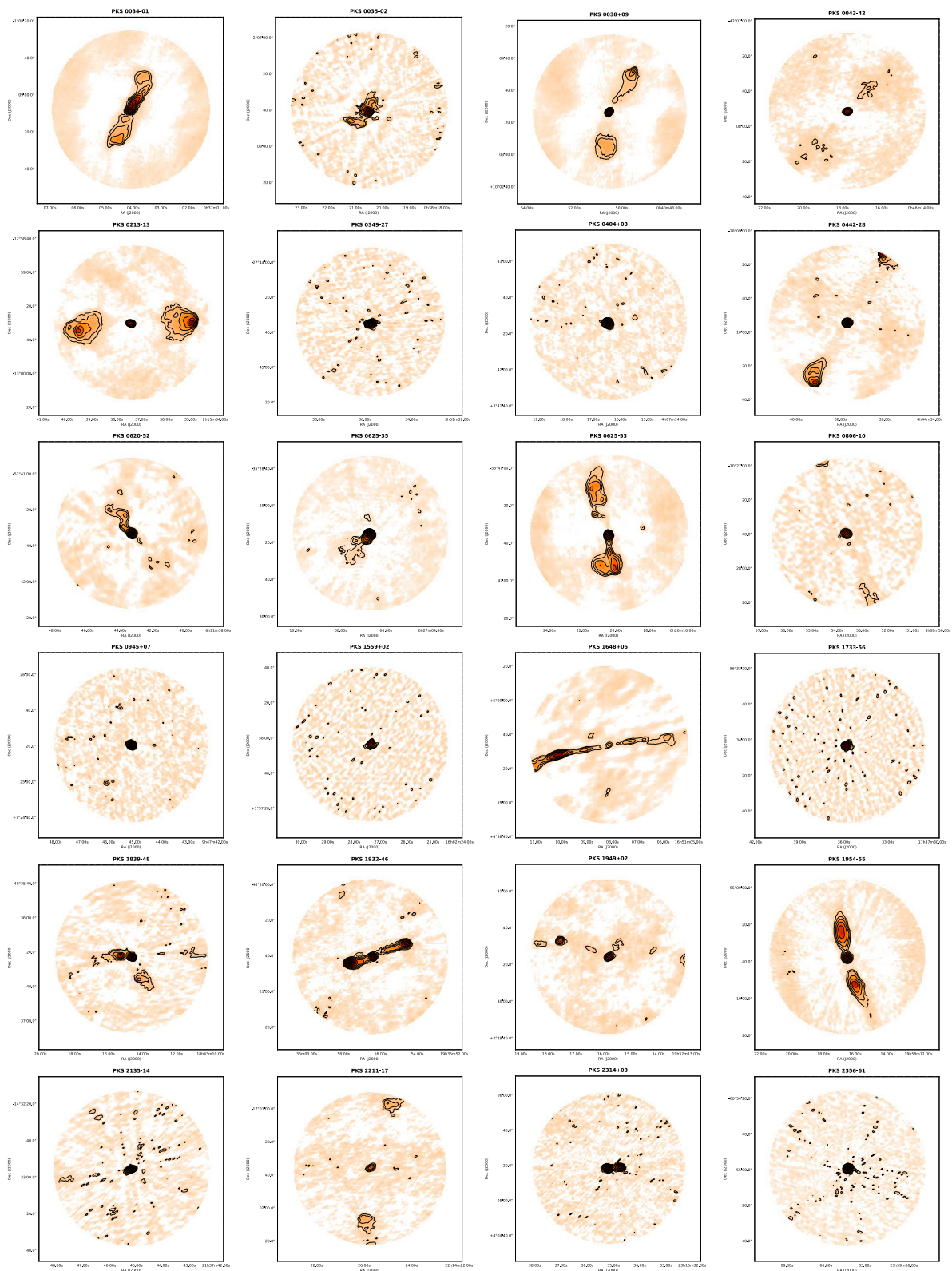**Figure A1.** – *continued*

Figure A1. *– continued*

Figure A2. Images of the mm continuum emission of 25 radio galaxies in the sample (the CSS/GPS objects – PKS1151–34, PHS1814–63, PKS1934–63 – are not shown, and the plot of PKS2221–02 is missing but the continuum is unresolved). Note that these images have not been corrected for the primary beam.
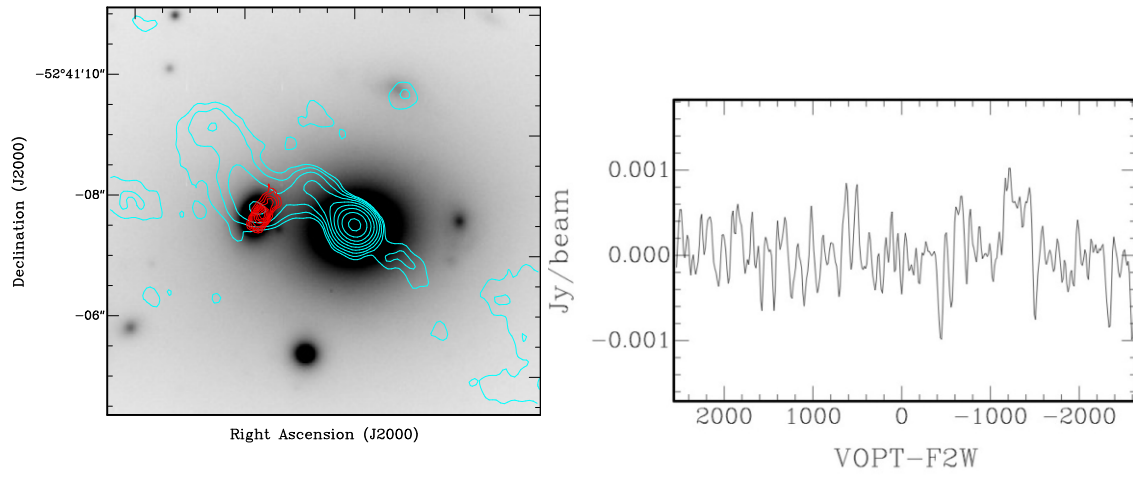
Figure A3. A possible jet–cloud interaction in PKS0620–52. Left panel: of H_2 surface brightness derived from the CO observations (red) overlayed on the r' optical image of Ramos Almeida et al. (2011) (grey scale), and the 3-mm continuum (cyan) for PKS0620–52. The molecular gas appears to be associated with a companion located, in projection, where the radio jet bends. Right panel: the CO(1-0) profile at the location of the emission.
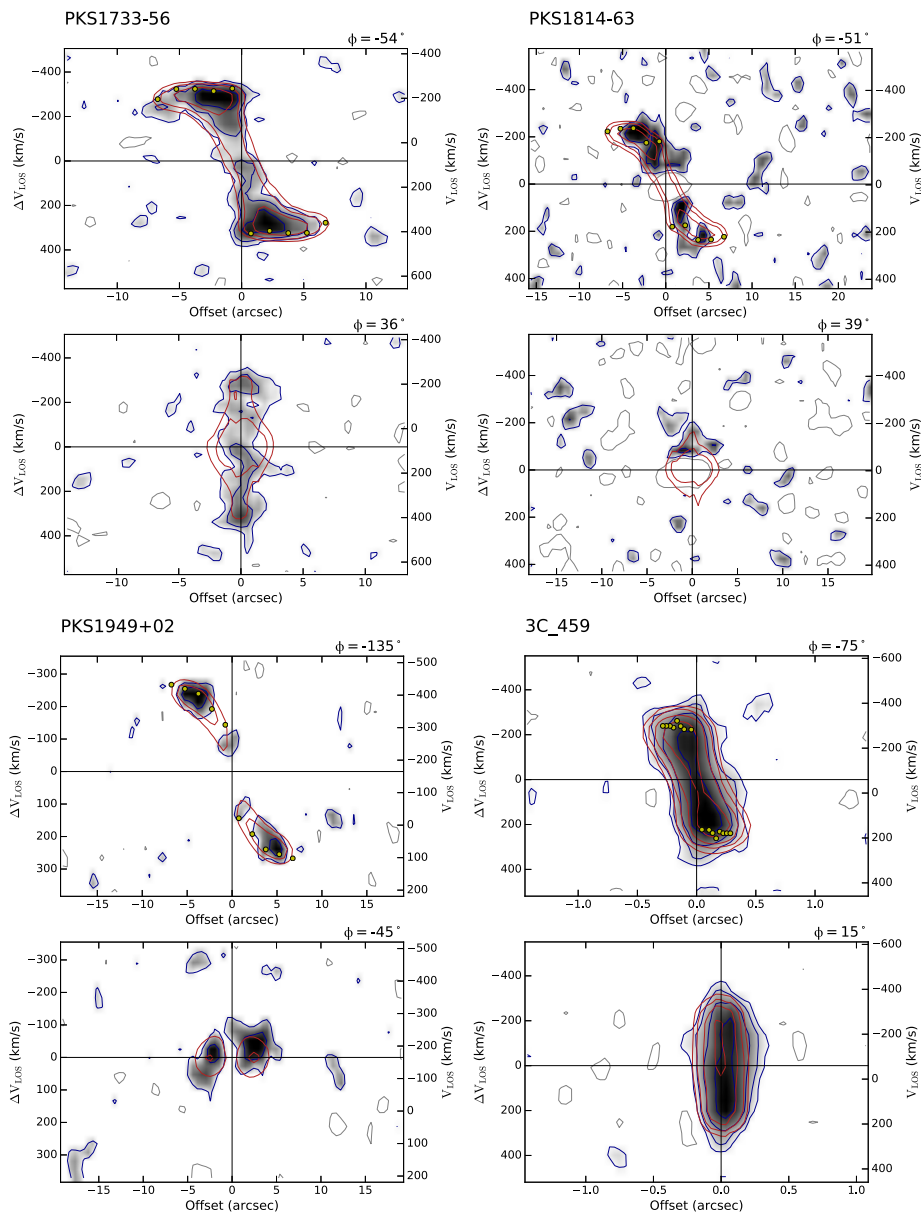
Figure A4. PV plots, taken along major and minor axis, from the modelling of the CO distribution using the 3D-Barolo software Di Teodoro & Fraternali (2015). The grey scale represents the data and the contours the model. The cube of 3C 459 is the one at higher spatial resolution from the ALMA archive: ADS/JAO.ALMA#2018.1.00739.S, PI Balmaverde.

This paper has been typeset from a TEX/LATEX file prepared by the author.